ISBN 91-628-2182-2
LUNFD6/(NFFL-7128) 1996

Data Base and Slow Controls System of the DELPHI VSAT and Two-Photon Physics using DELPHI at LEP

Thesis Submitted for the Degree of
Doctor of Philosophy in Physics
by

Ivan Kronkvist

Department of Particle Physics
Lund University
Professorsgatan 1
Box 118
S-221 00 Lund
Sweden

Data Base and Slow Controls System of the DELPHI VSAT and Two-Photon Physics using DELPHI at LEP

By due permission of the faculty of mathematics and natural sciences of the Lund University to be publicly discussed at the lecture hall B of the Department of Physics, October 18, 1996, at 10:15 a.m., for the degree of Doctor of Philosophy

by

Ivan Kronkvist

Department of Particle Physics
Lund University
Professorsgatan 1
Box 118
S-221 00 Lund
Sweden

This thesis is based on four papers, included as Appendices A to D:

A A Silicon-Tungsten Electromagnetic Calorimeter for LEP,
Nucl. Instr. and Meth. **A305** (1991) 320.

B The Database of the DELPHI Very Small Angle Tagger (VSAT),
DELPHI 92-116 (1992) PROG 190.

C The Slow Control System of the DELPHI Small Angle Tagger (SAT) and Very Small Angle Tagger (VSAT),
DELPHI 94-6 (1994) PROG 204.

D A Measurement of the Photon Structure Function F_2^γ at an Average Q^2 of 12 GeV^2/c^4,
Proceedings of the Photon '95 Internationl Workshop on Gamma-Gamma Collisions and Related Processes, Sheffield, UK, April 8-13, 1995.

Welcome to the World of Elementary Particle Physics

Abstract

This thesis is based on work done 1991-1996 using the DELPHI detector at LEP, and is summarized in four articles. It consists of four main parts.

The first part describes the Very Small Angle Tagger (VSAT) and Small angle TIle Calorimeter (STIC), which are sub-detectors of DELPHI. The VSAT consists of four silicon-tungsten electromagnetic calorimeter modules, having silicon strip planes for accurate position determination of the shower maximum. The modules are placed at ± 7.7 m from the DELPHI interaction point, two at each side, allowing detections of electrons and positrons in a polar angular range of 5 to 7 mrad. The STIC consists of two cylindrical electromagnetic calorimeters having scintillating tiles interspaced with lead absorbers, and is read out by optical fibers running orthogonal to the active planes. It is positioned 2.2 m from the interaction point and covers an angular region of 29 to 185 mrad in polar angle.

The second part describes the structure of the DELPHI data base, and how this was implemented for the VSAT detector. An automatic on-line calibration data base updating procedure that was set up in 1991 in order to prepare for off-line analysis and luminosity calculations.

The third part gives an introduction to the DELPHI slow controls system. This is a very complex system as a whole, and the implementation for VSAT showed need for detector specific software adapted to the custom built hardware. As an example on how the system can be used in tracing problems and their origins, there is a section on the radiation damage sustained to two of the VSAT modules in September 1995. There is also a description on how the Small Angle Tagger (SAT) slow controls system was adopted to the STIC detector in early 1994 when the STIC was installed replacing the SAT as the main DELPHI luminosity monitor.

The forth and final part is about two-photon physics at DELPHI, with emphasis on a VSAT double-tagged event analysis. Here is shown the feasibility of looking for double-tagged events where the scattered particles are tagged in very small angles. The cross section for such events is very small, but the findings of data is consistent with Monte Carlo predictions using a combination of VDM+QPM+(QCD-RPC) models, and demonstrates the feasibility of making such investigations with future DELPHI datataking.

Contents

Abstract I

Foreword 1

1 Apparatus 2
- 1.1 LEP, Large Electron Positron collider . . . 2
- 1.2 DELPHI . . . 4
  - 1.2.1 Micro Vertex Detector (VD) . . . 4
  - 1.2.2 Inner Detector (ID) . . . 4
  - 1.2.3 Time Projection Chamber (TPC) . . . 6
  - 1.2.4 Outer Detector (OD) . . . 6
  - 1.2.5 Forward Chambers (FCA,FCB) . . . 6
  - 1.2.6 High density Projection Chamber (HPC) . . . 7
  - 1.2.7 Forward ElectroMagnetic Calorimeter (FEMC) . . . 7
  - 1.2.8 Small angle TIle Calorimeter (STIC) . . . 8
  - 1.2.9 Very Small Angle Tagger (VSAT) . . . 10
- 1.3 Data Acquisition System (DAS) . . . 12
  - 1.3.1 Hardware . . . 12
  - 1.3.2 Software . . . 13
  - 1.3.3 Data Readout and flow . . . 13

2 Data Base of the VSAT detector 14
- 2.1 The DELPHI data base structure . . . 14
- 2.2 The structure of the VSAT data base . . . 18
  - 2.2.1 Geometrical constants of the VSAT . . . 18
  - 2.2.2 Calibration data base for VSAT . . . 20
  - 2.2.3 Slow Control data base for VSAT . . . 21
  - 2.2.4 On-Line Data Base updating program package (ODB) . . . 24

3 Slow Controls System 26
- 3.1 DELPHI Slow Controls System . . . 26
  - 3.1.1 Front-end Systems (G64) . . . 28
  - 3.1.2 VAX Systems . . . 29
  - 3.1.3 Ancillary Systems . . . 32
- 3.2 VSAT Slow Controls System . . . 34
  - 3.2.1 BIAS system . . . 34

3.2.2 SWST system . . . 35
3.2.3 FB System . . . 35
3.2.4 GSS Systems . . . 36
3.2.5 SMI States, Actions and Recoveries . . . 36
3.2.6 Radiation Damage to the VSAT detector . . . 38
3.3 STIC Slow Controls System . . . 40
3.3.1 BIAS and FB systems . . . 41
3.3.2 POSI system . . . 41
3.3.3 TEMP system . . . 42
3.3.4 HV_V system . . . 42
3.3.5 GSS Systems . . . 42
3.3.6 SMI States, Actions and Recoveries . . . 43

4 Two-Photon Physics 45
4.1 Theoretical Background . . . 46
4.1.1 Processes . . . 46
4.1.2 Kinematics . . . 48
4.1.3 Models . . . 48
4.1.4 Cross Section . . . 52
4.1.5 The Photon Structure Function . . . 55
4.1.6 Experimental Techniques . . . 57
4.2 Two-Photon Physics at DELPHI . . . 58
4.2.1 Results of No-Tagged Data Analysis . . . 59
4.2.2 Results of VSAT Single-Tagged Data Analysis . . . 60
4.2.3 Measurement of the Photon Structure Function . . . 60
4.2.4 Double-Tagged Two-Photon Data analysis . . . 61

Acknowledgements 71

Bibliography 72

A A Silicon-Tungsten Electromagnetic Calorimeter for LEP 75

B The Database of the DELPHI Very Small Angle Tagger (VSAT) 89

C The Slow Control Systems of the DELPHI Small Angle Tagger (SAT) and Very Small Angle Tagger (VSAT) 100

D A Measurement of the Photon Structure Function F_2^γ at an Average Q^2 of 12 GeV$^2/c^4$ 108

Foreword

This thesis summarizes the work I have done, as a graduate student, in the DELPHI Collaboration for the last five and a half years. Only the successes are accounted for; the large number of misstakes and side-tracks experienced have little or no interest the rest of the world, although they were very educational for me.

The first article at the end of the thesis, included as appendix A, contains a description of the VSAT detector. The next two articles, Appendices B and C, are the results of my work. Appendix D contains my contribution to the proceedings of **Photon '95**, the Xth International Workshop on Gamma-Gamma Collisions and Related Processes, held in Sheffield, UK, 8-13 April, 1995. The text preceding the articles contains background information on the DELPHI detector, the data base and slow controls systems, and relevant theory for my physics analysis.

My first encounter with elementary particle physics was in high-school, where my physics teacher, a former particle physicist himself, held a short voluntary course in the field, ending with a (free) visit to DESY, Hamburg. After finishing high-school my mind was already set on pursuing a Ph.D. in particle physics, and here I am, the ultimate goal of my life fulfilled. Along the way I got introduced to CERN as a summer student in 1990, and when I in December 1990 was accepted as graduate student at the Department of Elementary Particle Physics, Lund University, I moved to Geneva and spent two years at CERN working mainly with the on-line system of the VSAT detector. This work included setting up an automatic data base updating procedure (Appendix B) and installing the slow controls system for VSAT (Appendix C).

In 1993, after coming back to Lund, I got involved in initial tests of the new STIC detector, helping to construct a platform to be used in the test beam line. As an expert in the DELPHI slow controls system, I also got the opportunity to assist in setting up the slow control system for STIC.

After my part in the STIC project was done, I turned to analyzing DELPHI two-photon data, using the VSAT detector to tag the scattered beam leptons of the events. At the Photon '95 conference I was chosen by the DELPHI Speakers Bureau to report on a measurement of the Photon Structure Function F_2^γ (Appendix D), and concentrated after that on the double tag analysis.

To finally summarize my views of these past five and a half years, I'd like to say that it was an interesting time. I have made a lot of friends from all over the world and learned many things, not only in the field of elementary particle physics.

Ivan Kronkvist
Lund, August, 1996

Chapter 1

Apparatus

At LEP, the Large Electron Positron collider, there are four experiments operating, one of them called DELPHI, DEtector with Lepton, Photon and Hadron Identification. This chapter gives a brief introduction to LEP and the subdetectors of DELPHI. Emphasis is put on describing the Small angle TIle Calorimeter, STIC, and Very Small Angle Tagger, VSAT, subdetectors in whose on-line systems much of my effort has been put.

A short description of the DELPHI data acquisition system is also included in this chapter.

1.1 LEP, Large Electron Positron collider

LEP is an e^+e^- collider with a circumference of 26.7 kilometer. Thus, it is the largest collider ever built. It was designed by physicists and engineers from CERN and built by the European industry in the years 1982 to 1989. The construction cost was 1300 million Swiss francs which was contributed by the 14 member states. The machine was ready for physics in the summer of 1989 and the pilot run took place on August 14 same year.

The LEP tunnel is placed outside Geneva, at the border between Switzerland and France. The machine consists of eight straight 500 m sections connected by eight 2800 m arcs with a radius of curvature of 3300 m. Underground depth varies between 50 and 175 m, and the tunnel has a gradient of 1.4 % with respect to the horizontal plane, the lowest point being closest to Geneva. As the vertical shafts were very costly to make, the length of tunnel that lies under the Jura mountains was minimized and giving the tunnel a small slope saved a lot of money when it was excavated. The inside diameter of the tunnel is 3.8 m in the arcs and 4.4 or 5.5 m in the straight sections depending on the plant installed in them. The four large experimental halls have diameters of 23 m and lengths of 80 m.

After an acceleration phase in the PS and SPS the electrons and positrons are injected in to LEP. During the last few years, the schemes of injections have changed from at first having four equally interspaced bunches in LEP, to eight equally interspaced bunches, and finally to having four *bunch-trains* that are equally interspaced, where each consist of two to four mini-bunches, *wagons*. All these changes have lead to an increase of the luminosity and thus to higher data-taking rates for the experiments. Each bunch in the first two schemes consisted of about 10^{11} particles, corresponding to a current of 3 mA

per circulating beam. In the bunch-train scheme, the number of particles in a wagon is about half of a 'normal' bunch and thus this scheme is only beneficial if there are more than two wagons in each train.

In LEP the particles are accelerated from an initial energy of 20 GeV up to about 46 GeV (LEP100) where they are kept for several hours. At the interaction points the beams are strongly focused to have elliptical cross-sectional areas of about 210 μm in width and 8 μm in height. The longitudinal length of a bunch is around 1.1 cm. The energy loss due to synchrotron radiation, about 120 MeV per rotation at 46 GeV, is compensated for by acceleration cavities situated at two straight sections of LEP.

The nominal luminosity of $1.6 \cdot 10^{31}$ cm^{-2}s^{-1} was not reached during the first years of operation, but with the new bunch-train scheme the machine runs steadily with luminosities around or even above the nominal value for hours.

In the last running period in 1995, LEP was run with beam energies around 70 GeV as a test for the next phase, LEP200. Starting in 1996 LEP will enter the LEP200 phase and eventually run with more than 90 GeV beam energies to allow detailed study of W^+W^- production as well as searches for new particles, *e.g* supersymmetric and Higgs particles.

"PARTICLES, PARTICLES, PARTICLES."

1.2 DELPHI

The DELPHI [1] detector is shaped as a cylinder with the beam pipe along the cylinder axis, figure 1.1. It has a length of 10 m and radius of 5 m. It is divided into a cylindrical *barrel* part and a conical *end-cap* part on each side of the barrel. The transition regions between these parts, at polar angle 43° and 137°, are partially obscured by cables and connectors. During the technical stop in November 1994 to April 1995 scintillators were installed in these regions to fill the holes. The end-caps can be moved along the beam pipe and away from the barrel to open up DELPHI and allow for maintenance work on the sub-parts of both barrel and end-caps. A superconducting solenoid of radius 2.6 m is installed within the barrel to provide a uniform magnetic field of 1.2 T along the beam pipe.

As the name DELPHI suggests, DEtector with Lepton, Photon and Hadron Identification, special emphasis has been put on powerful particle identification. It consists of around 20 sub-detectors and a brief description will be given below for the parts of main interest to the work of this thesis, *i.e.* the charged particle tracking system and electromagnetic calorimeters.

1.2.1 Micro Vertex Detector (VD)

Initially, the Micro Vertex Detector [2] consisted of two cylindrical layers of silicon strip detectors surrounding the beam pipe at radii 9 and 11 cm. The length of the layers is 23.6 cm giving an angular coverage of 37° to 143° in θ. In 1991 the detector was upgraded by installation of a third layer at radius 6.3 cm. This layer has a length of 20.8 cm.

Each layer consists of 24 modules with a 10° overlap and each module consists of four segments in z. Three $R\phi$-points are measured for each track passing the detector and the intrinsic $R\phi$-resolution is 8 μm.

In 1994 the layers at radii 6.3 cm and 11 cm were equipped with double sided silicon strip detectors in an attempt to measure the z-coordinate in addition to the $R\phi$ of a hit. A precision of 18 μm in z averaged over all incident angles has been achieved.

1.2.2 Inner Detector (ID)

The Inner Detector [3] is a tracking and triggering detector. It consists of two concentric layers, a jet chamber and the trigger layers (TL). The jet chamber is a driftchamber having an inner radius of 12 cm, outer radius of 22 cm, and a length of $|z|= 80$ cm. It is subdivided into 24 sectors of 15° in ϕ, each having 24 sense wires, measuring drifttime. The single wire resolution is of the order of 90 μm. The two-track separation is around 1 mm. The trigger efficiency for the jet chamber is above 90% for jet events.

The TL has an inner radius of 23 cm, outer radius of 28 cm, and a length of $|z|= 50$ cm. It consists of five cylindrical MWPC, each equipped with 192 anode wires parallel to the beam axis, and 192 cathode strips forming full circles at constant z. The geometry of the strips in the five layers is projective towards the interaction point. Full angular coverage is down to 30° (150°) in θ. The $R\phi$ measurement is mainly used in the trigger and for resolving the left/right ambiguity in the JET chamber. On well isolated tracks, the single-

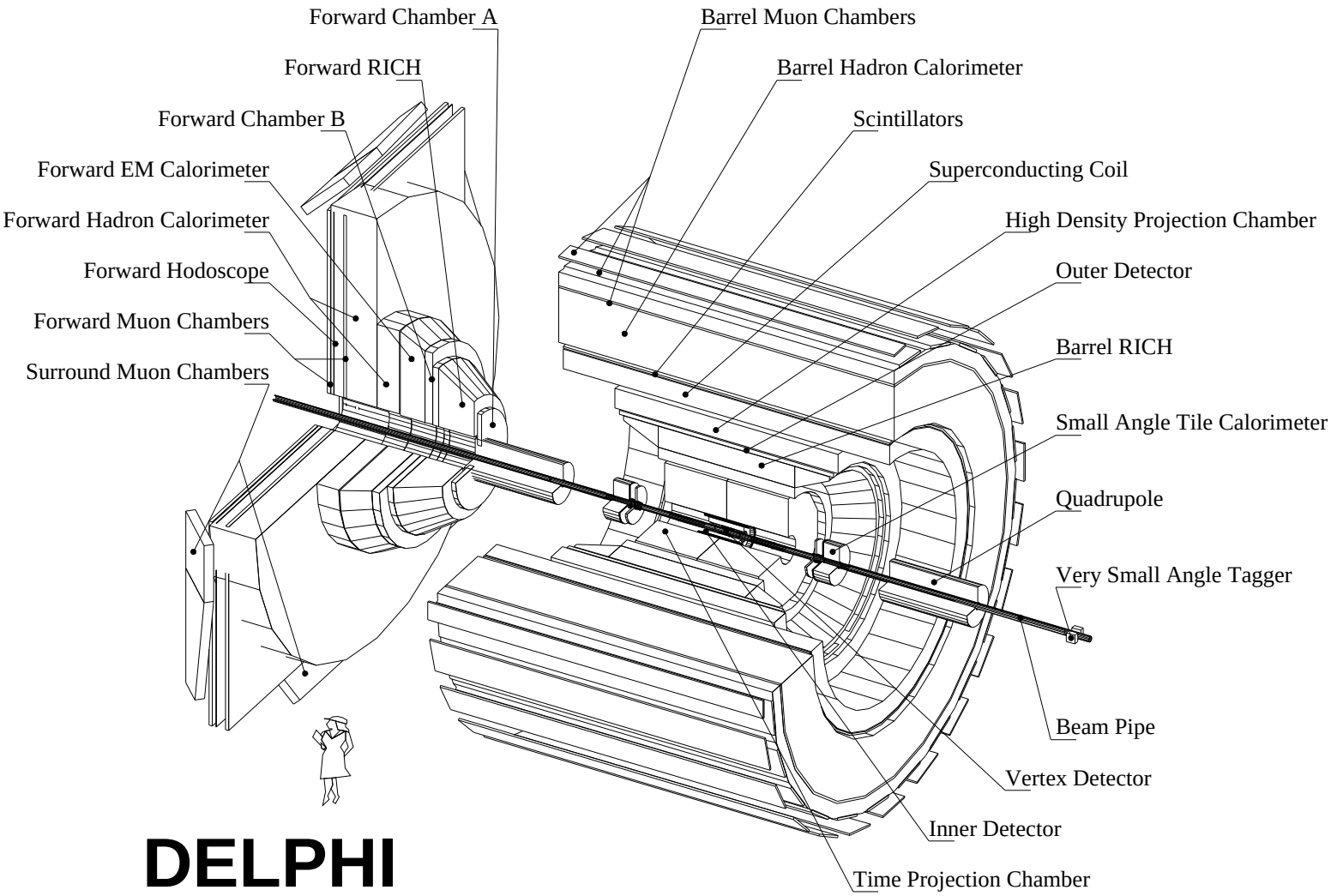

Figure 1.1: The DELPHI detector with its subsystems indicated

plane z-resolution depends on θ and ranges from 0.5 mm (at 90°) to 1 mm (at 30°). The trigger efficiency for the trigger layers is $> 95\%$ for single tracks.

1.2.3 Time Projection Chamber (TPC)

The Time Projection Chamber [4] is the central tracking device of the DELPHI experiment. It was designed for good tracking abilities, and provides a particle identification by dE/dx, in particular e/π separation below 8 GeV.

It consists of two cylindrical parts, placed on each side of the interaction point along the the beam pipe, separated by a central drift anode. Each part has an active length of 134 cm, with inner and outer radii of 32.5 and 116 cm respectively. The circular end-caps are subdivided into 2×6 sectors in ϕ equipped with 16 radial pad rows and 192 sense wires.

The space point determination is done assuming Gaussian shape of the signals over adjacent pads. For tracks with p_{bot} greater that 1.5 GeV/c the average resolution is 230 μm in $R\phi$ and 900 μm in z.

The Ring Imaging CHerenkov detector (RICH) was dedicated for particle identification, but is of no concern to this thesis.

1.2.4 Outer Detector (OD)

The Outer Detector [5] is the outermost tracking device in the DELPHI barrel. Its inner and outer radii are 1.97 and 2.08 m respectively, and its active length is 4.5 m. It consists of 3480 individual 1.65×1.65 cm^2 drift tubes arranged in 24 modules of five layers each, mounted on the Barrel Ring Imaging CHerenkov detector (BRICH).

To ensure full azimuthal coverage there is an overlap of adjacent modules. The coverage in θ is between 37° and 143°. All five layers measure the $R\phi$ coordinate of a track to a resolution of 110 μm. In addition, three layers also give a fast z measurement by relative timing of signals from both ends with a resolution of 4.4 cm. The OD gives extra precision for the momentum determination of high momentum tracks.

1.2.5 Forward Chambers (FCA,FCB)

The Forward Chambers are the tracking detectors in the DELPHI forward regions. They provide powerful tracking and triggering in the angular region of $11° \leq \theta \leq 33°$.

Chamber A [6] is mounted on both ends of the TPC. One side consists of three chambers, each with two staggered layers and split into half disks with an outer radius of 103 cm. The chambers are turned with respect to each other by 120°, thus providing 2×3 coordinates. The layers are constructed from extruded conductive plastic forming square cells with a 100 μm anode wire in the middle. A double layer is reinforced on both outer surfaces by 0.7 mm G10 sheets. These sheets carry a pattern of 58 mm wide cathode strips, rotated by $\pm 60°$ with respect to the corresponding anode wires.

Chamber B are positioned between the Forward Rich Imaging CHerenkov detector (FRICH) and the Forward ElectroMagnetic Calorimeter. A complete disk is a regular dodecagon with inner and outer radii 48 and 211 cm respectively. There are 12 sense

wire planes, separated by 1.1 cm, which are rotated in pairs by 120° with respect to each other. The wire planes are tensioned on G10 frames and separated by cathode planes made of 1 mm thick conducting G10 containing carbon dust. Separate endplates close the gas volume. The sense wires have a spacing of 2 mm and separated by field wires.

The resolution of Chamber A is 300 μm per layer and that of Chamber B is 290 μm per layer. Combining the 12 layers of Chamber B gives a resolution in x and y of 130 μm.

1.2.6 High density Projection Chamber (HPC)

The High density Projection Chamber [7] is the electromagnetic calorimeter of the DELPHI barrel. It is a sampling calorimeter using a projection chamber approach which gives a good energy resolution together with a complete representation of the energy flow, and it is one of the first large scale applications of this idea.

The detector consists of 144 modules arranged in 24 sectors with 6 modules each along z. Each module consists of a converter/drift structure and a single plane active detector. The converter forms a large volume gas sampling structure which is mechanically self-stable. The primary ionization from a shower is drifted along the sampling slots to a proportional wire chamber.

The converter walls are made of thin trapezoidal lead wires glued to both sides of a flat fiberglass epoxy substrate of 100 μm thickness. There are 40 lead walls in each module which gives a total lead thickness og 19 radiation lengths. The 8 mm gap between the walls constitute the drift chambers. The drift field is provided by a voltage gradient between neighbouring lead wires in the converter wall. The $R\phi$ coordinates are sampled by pad readout of the proportional chamber, nine samples in shower depth and 1° in azimuth.

A study [8] has shown that for the 1990 data the energy resolution of the HPC was given by $\sigma_E/E = 25\%/\sqrt{E} + 7\%$ (E in GeV) where the second term is due to energy loss in the material in front of the HPC, leakage, gas saturation, calibration fluctuations instabilities *etc.*

1.2.7 Forward ElectroMagnetic Calorimeter (FEMC)

The Forward ElectroMagnetic Calorimeter [9] is, as the name suggests, the calorimeter covering the forward region of DELPHI. It consists of two 5 m diameter disks of SF3 lead glass counters, covering the angular regions $8° \leq \theta \leq 37°$ and $143° \leq \theta \leq 172°$. The counters consists of blocks of truncated pyramidal shape, arranged to provide a "quasi-pointing" geometry. Each disk consists of 4532 counters mounted in 64 stainless steel boxes, each box containing 80 counters arranged in ten columns of eight blocks each. The boxes on the periphery of the disks contain the number of blocks appropriate to the circular geometry. The counters are 20 radiation lengths deep, and read out with vacuum phototriodes.

The angular resolution is about $1° \times 1°$. At LEP the energy resolution for Bhabhas at 45 GeV has been measured to be 6%, using calibration constants from test beam results. By using part of the data to correct the calibration constants the energy resolution improved to 4%.

1.2.8 Small angle TIle Calorimeter (STIC)

In mid 1992 a project started to equip DELPHI with a new luminosity monitor, to replace the old Small Angle Tagger (SAT). The main goal was to improve the systematic contribution from the luminosity determination to be below 0.1% in order to match the statistical uncertainties in the determination of the hadronic cross section at the Z^0 peak. As a result of this, the Small angle TIle Calorimeter was designed and installed in time for the 1994 run [10].

The STIC detector consists of two calorimeters located at ± 220 cm from the interaction point, figure 1.2, covering the polar angular regions between 29 and 185 mrad. Each calorimeter is divided into two half-cylindrical modules. Longitudinally they are divided into 47 sampling layers plus two silicon pad layers placed at 4 and 7.4 radiation lengths respectively. A veto counter, composed of two scintillator planes, covers the front of the calorimeters to allow $e\gamma$ separation and provide a neutral energy trigger. Also in one arm of the STIC there is a tungsten mask which is used for defining the inner edge of acceptance for Bhabha scattering, figure 1.3.

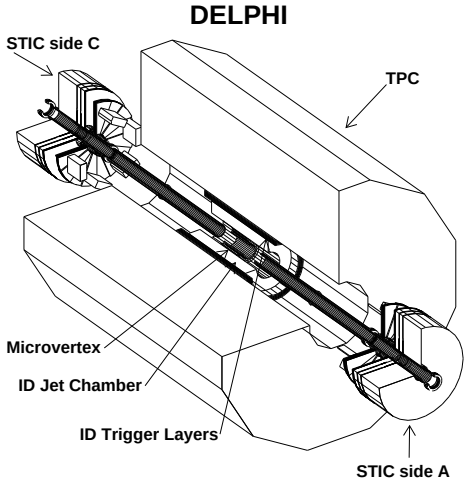

Figure 1.2: The placement of the STIC detector inside the DELPHI barrel.

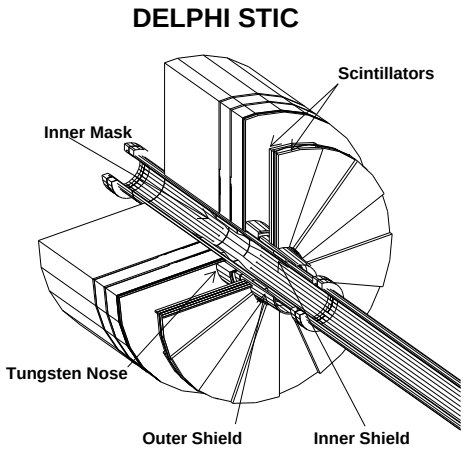

Figure 1.3: The STIC detector setup.

Each sampling layer is made of 3.4 mm stainless steel laminated lead plates and 3.0 mm polysterene based scintillator as active media, for a total thickness of 27 radiation lengths. To avoid cracks in the detector the lead absorber forms a continuous plate, while the scintillator planes are made of tiles, which are optically separated by 120 μm thick white Tyvek[1] paper that acts as diffuser. The tiles are arranged into eight azimuthal sectors (22.5° wide) and ten radial sectors for a total of 80 towers per module. The geometry of the towers is projective towards the interaction point, figure 1.4.

The readout is made by 1 mm optical fibers doped with Y7 green wavelength shifter, running orthogonal to the active planes and grouped together towerwise at the back of the calorimeter by a clamp fixed on a supporting plate. Energy response fluctuations over

[1] Tyvek© is Du Pont's registered trademark for its spunbonded olefin

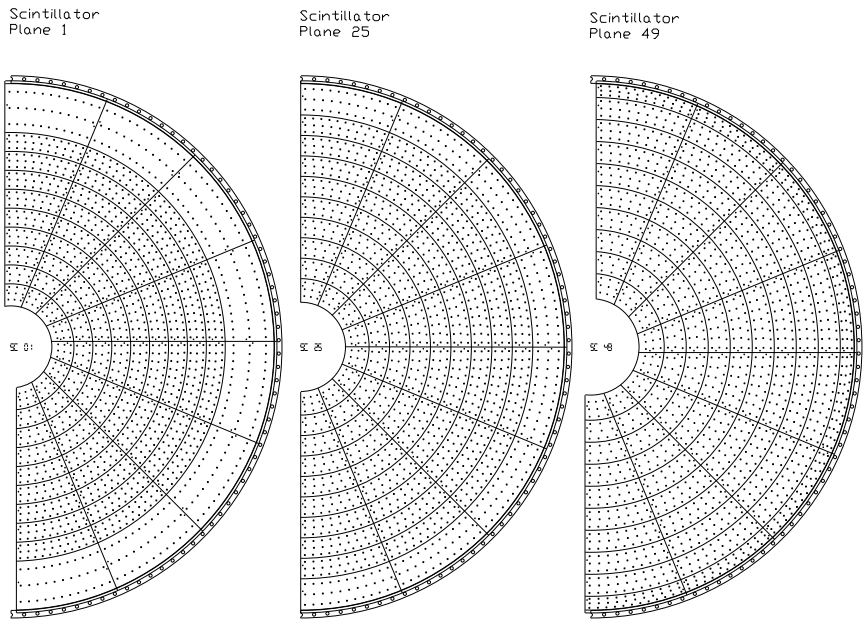

Figure 1.4: Three planes of the STIC calorimeter, at different depth, indicating the projective geometry of the towers.

the calorimeter surface were minimized by choosing a suitable combination of continuous absorber plates and optimal fiber density (about 1 fiber/cm^2).

The fiber bundles from each tower are read out by 1" phototetrodes, placed after a 5 mm air gap. The reason for chosing phototetrodes is their ability to operate inside high magnetic fields. Charge preamplifiers and high voltage dividers are mounted inside light tight aluminium cylinders which hold each tetrode.

The Veto system consists of 64 trapezoidal scintillation counters arranged into two planes in front of each calorimeter. The counters are made of 10 mm thick plastic scintillators and the light is collected at the edges by bundles of WLS fibers and taken out of the magnetic field by 10 m long clear optical fibers to be collected by 10 stage photomultipliers. The response of the Veto counters is around 20 photoelectrons per MIP. Asking a MIP requirement on both counters, testbeam measurements give an efficiency of $\geq 99.7\%$ for charged particle identification and a loss of neutral triggers of around 5% due to calorimeter albedo.

The silicon pad layers consist of single-sided AC coupled FOXFET silicon strip detectors. The thickness of the planes is 300 μm, and the readout strip pitch is 1.712 mm in the first plane and 1.754 mm in the second plane to match the projective structure of the calorimeter. For each of the two planes there are two rows of pads, figure 1.5. The first one covers a radial region from 7.15 to 11.3 cm and is divided into 45° pads with two 24-strip sectors. The second row covers the radial region of 11.3 to 18.03 cm and consists of 22.5° 36-strip pads.

Due to the optical fibers for the calorimeter readout, it is necessary to have holes

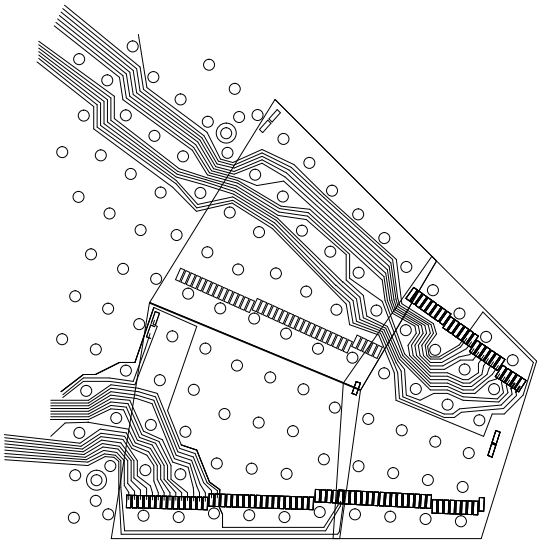

Figure 1.5: A 45° sector of the silicon strip detectors (the strip structure is not shown).

(1.4 mm diameter) in the silicon pads to let the fibers through. A laser beam was used for the drilling and the precision of the edge cut is 10 μm. The overall precision of the silicon detector geometry is within 5 μm.

The deviation of energy linearity of the calorimeter response is within $\pm 1\%$ and the energy resolution is 2.7% at 45 GeV. The Silicon detector gives an angular resolution of 13 mrad.

1.2.9 Very Small Angle Tagger (VSAT)

The Very Small Angle Tagger [11] is an electromagnetic calorimeter that measures the LEP luminosity at very small angles, between 5 and 7 mrad. At its small angle position it has a very high cross section for the Bhabha scattering process, thus obtaining a high statistical precision. It is, however, quite sensitive to background conditions, beam parameters, and to the precision by which the exact geometry of the detector and the beam transport are known.

VSAT was originally designed to give a fast online value for luminosity, as well as fast beam position measurements. These criteria are fulfilled, and in addition, the signals from the VSAT are read out into the main DELPHI data stream thus enabling other uses for it, *e.g.* as a tagger for $\gamma\gamma$ events where either one or both of the scattered beam leptons are seen in the VSAT, see chapter 4.

The detector consists of four modules, placed 7.7 m away from the interaction point downstream of the superconducting quadrupole magnets, at an elliptical section of the beam pipe, figure 1.6. The superconducting quadrupole magnets in front of the VSAT have a focusing effect in vertical and defocusing effect in horizontal direction, which distorts the VSAT (θ, ϕ)-acceptance. The ϕ coverage is $\pm 45°$ at 45 GeV, and it increases for lower energies due to the quadrupole focusing.

Each detector module have a width of 3.2 cm, height of 5 cm and a depth on 24

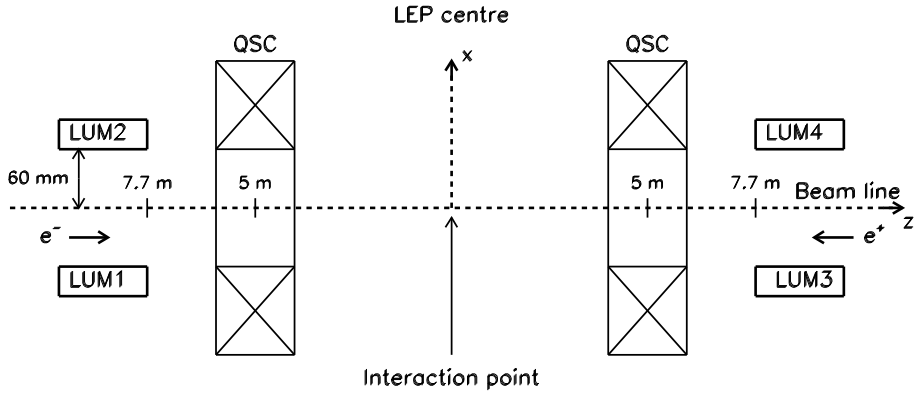

Figure 1.6: The placement of the four VSAT modules from a top view of LEP.

radiation lengths. It is a sandwich type calorimeter with tungsten absorbers interspaced with silicon planes for the readout. There are twelve silicon full area detector (FAD) planes equally spaced throughout the modules and three silicon strip planes, two x-planes and one y-plane, close to the shower maximum to measure the position of the incoming particle. The pitch of the strips is 1 mm. Figure 1.7 shows the actual placements of two modules at the elliptical beam pipe on one side of the interaction point, and figure 1.8 shows the internal layout of each module.

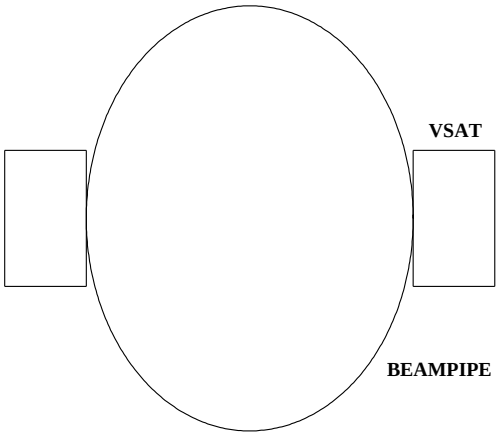

Figure 1.7: The placements of the two VSAT modules at the elliptical beam pipe.

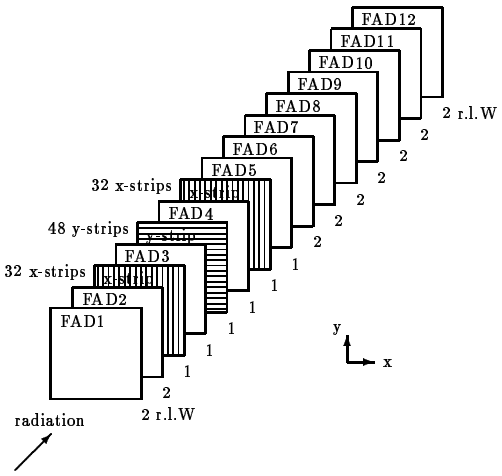

Figure 1.8: The internal layout of a VSAT module, showing the absorber and readout planes.

The strip information is used for eliminating showers being too close to a calorimeter edge, thus to eliminate mismeasures due to energy leakage. The resolution on the reconstructed position is 200 μm and the energy resolution is $35\%/\sqrt{E}$.

The VSAT provides three kinds of triggers:

- A Bhabha trigger, which is an event with a coincidence between diagonal modules, each module detecting at least 20 GeV.

- Bremsstrahlung off-momentum beam particles, recorded by a downscaled trigger, also having an energy threshold of 20 GeV.

- Accidental Bhabha coincidences, recorded by a trigger requiring an off-momentum e^+/e^- in an inner module and another one in the diagonal (outside) module N bunches later (N being the number of bunches in LEP).

Since the VSAT trigger rate is higher than the DELPHI rate, VSAT events are accumulated in a local event buffer which is read out at each DELPHI event. However, if the buffer gets full, a DELPHI event is forced by the VSAT to insure that no VSAT data is lost. Though this happens very rarely.

When LEP enters the new phase with higher energies, the VSAT event rate will be even more dominant over the DELPHI rate, since LEP will leave the Z^0 peak and the e^+e^- annihilation cross section goes down. Because of this there may be a need of reducing the DELPHI deadtime caused by the VSAT trigger rate of the accidental coincidence triggers. This can be done by not reading out the first off-momentum particle and instead only flag it internally and wait for the second particle N bunches later, which will then be read out.

1.3 Data Acquisition System (DAS)

As many DAS's of complex experiments, the DELPHI DAS has a tree-like structure, where each level forms an elementary cell. The cells consist of two sets of buffers (source and destination), a transfer process and a control process. The task for each cell is to transfer data from the source buffer to the destination buffer. At each level there are generally more source than destination buffers, such that each level merges data.

The DELPHI DAS [12] contains 6-7 levels of elementary cells; the front ends, the board processing, the crates, the partitions, the central partition, the emulators and data logging.

1.3.1 Hardware

The DELPHI readout is built around a Fastbus embedded processor called Fastbus Intersegment Processor (FIP). It is based on a Motorola 68020 processor running at 16 MHz. It has 1.5 Mb of dynamic RAM, 256 kb of static RAM dual ported between the processor and a Fastbus slave port. The FIP is equipped with a Ethernet-Cheapernet port. It houses 1 Mb of EPROMs containing the OS9 operating system, the communication packages as well as development tools (editor, compiler, linker *etc*). DELPHI uses about 70 FIPs.

The DELPHI online cluster consists of 3 bootnodes and a set of VAX workstations 4000 called equipment computers (EC). Each EC is in charge of the control and monitoring of one or two partitions. It is connected to the Fastbus via a CERN Fastbus Interface (CFI).

1.3.2 Software

Each of the individual partitions, as well as the central run control, are managed by the State Manager [13] concept. In this concept, the experiment is described in terms of *objects*, *i.e.* logical subsystems, for each of which a number of *states* are defined. An object may correspond directly to a concrete entity in the experiment (a computer controlled device) or an abstraction used in describing the experiment provided it can be identified by a 'noun', *e.g.* 'run', 'trigger', 'central detector', *etc.*). The control system, which is given by the interaction between various objects, is specified using a formal language called *State Manager Language*.

1.3.3 Data Readout and flow

The data is transfered from the detector into digitization modules in a purely hardware process. It is then sent to the Front End Buffers (FEB)[2].

The Front End Buffers are read out by Crate Processors (CP). The CP is sitting at the interface between the trigger control system and the DAS and coordinates the readout with the LEP beam crossing. It performs data formatting and some first processing, *e.g.* channel reordering, pedestal subtraction, preparation for third level trigger.

The Crate Processors are supervised by the Local Event Supervisor (LES). The LES merges the data and formats and links it into its final ZEBRA structure. A decision is taken, according to user-defined criteria, whether the event is worth further processing. The LES is driven and supervised by a software running in the equipment computer.

The Global Event Supervisor (GES) controls the LESs of those partitions that participates in the central readout. It runs under the supervision of a software running in the main acquisition computer. The GES transfers the data from the LES to its own buffer and performs the final formatting of the data, which is now ready for logging onto mass storage by the main acquisition computer.

[2]In cases of detectors with large number of channels, a second level of buffering has been added, called Board Event Buffer (BEB).

Chapter 2

Data Base of the VSAT detector

The VSAT detector was included into the DELPHI data taking environment in the end of 1990, at which time the *data acquisition* and *data monitoring* programs existed. In 1991 it was time to set up the *On-line Data Base updating* (ODB) system for the detector.

In short, the ODB system is to ensure that the status and threshold values of the readout channels are at hand in time for the general processing of DELPHI raw data. These values may change during data taking, *e.g.* the noise on some or all channels may increase or decrease depending on other electrical systems such as LEP and other sub-detectors of DELPHI, or the signal from a strip in the detector may disappear completely and this should then be taken into account when the data is analysed.

This chapter will describe the ODB system and give a background introduction to the general DELPHI designs and requirements. First there is a description of the general structure of the DELPHI data base, then the VSAT data base structure, followed by an explanation on how the updating program works.

2.1 The DELPHI data base structure

In all experiments in any field of science it is necessary to know everything that can effect the results, especially so if one wants to claim good accuracy in the measurements. In large experiments, like DELPHI, with around 200,000 readout channels it is difficult to keep track of all parameters like calibration constants, thresholds, geometry *etc.* of each channel. To make it easier one creates a data base where all parameters are collected according to certain rules that make it easily manageable. Thus a data base is a searchable collection of numbers needed for understanding of the experiment output data.

In the early days of DELPHI planning it was decided to construct a dedicated data base system within the group, rather than using a commercial product. Therefore, a user friendly Hierarchical Data Base Manager, *CARGO*, was created. The programming language used was FORTRAN77, and the program package has since been developed to run on a wide range on computers systems (VAX VMS and ULTRIX, DEC Alpha stations, IBM VM/CMS, IBM RISCstations, NORD, CRAY, Hewlett Packard 9000, Apollo, Aliant, Convex, Sun, transputers *etc*).

The CARGO [14] Package consists of a set of files:

- one direct access *system file* in which the data structures to be used are defined;

- a number of corresponding direct access *data files*;
- a set of ASCII files for data exchange between different computers.

Users access the data base information through the direct access system and data files. The Hierarchical Data Base, supported by CARGO, might be represented by figure 2.1.

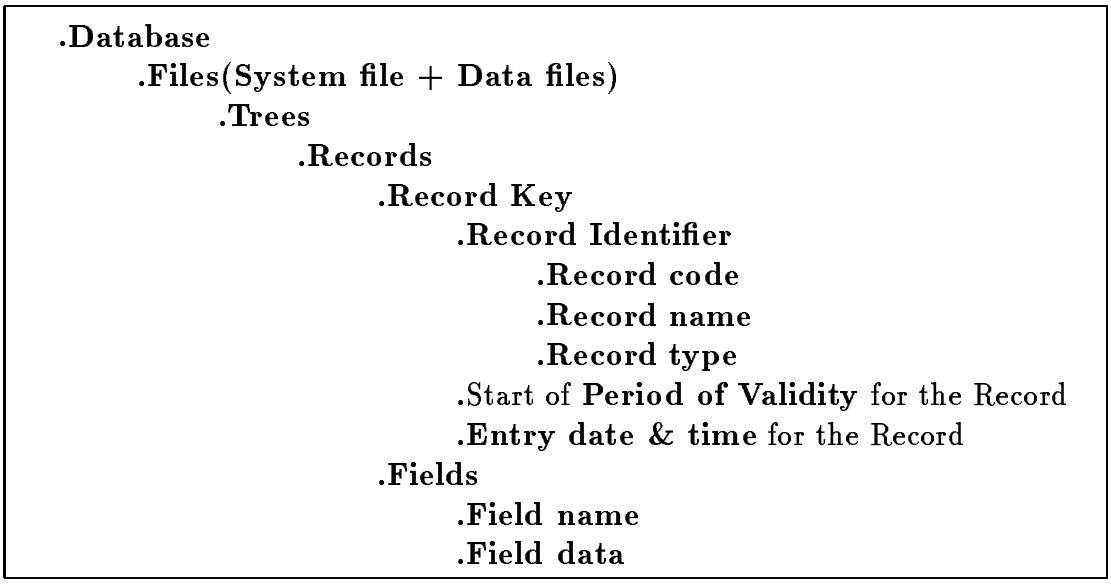

Figure 2.1: The Hierarchical Data Base

Currently the DELPHI data base consists of seven data files:

- *Data base Definition* file (system file);
- *Calibration & Detector Status Information* file which contains calibration and status information for all subdetectors of DELPHI in the `CALB` tree [15];
- *Geometry and Materials Constants* file which contains the geometrical constants in the tree `GEOM`, and constants about the materials used in DELPHI in the `MATC` tree [15];
- *Miscellaneous small data* file which contains the `MISC` tree;
- *Online RUN+TAPE Log* file containing information about the data taking conditions in the `BKON` tree;
- *Slow Control Data* file which contains all parameters necessary for the Slow Control system in the `SLOW` tree;
- *LEP Machine Parameter and Luminosity* file containing information from LEP control room about the beam, as well as the luminosity measured by DELPHI, in the `LEPM` tree.

The data in each tree is divided into records. The structure is such that each record name contains an acronym for the subdetector that it represents and the data for that detector is then divided into subparts, *e.g.* a fictitious detector `DET*` consisting of two segments, `SEG1` and `SEG2`, and has two types of sensing device, called `WIRE` and `PADS`, connected to each segment would be as is shown in figure 2.2. The sensing device records will then contain parameters specific to each channel, wire or pad in our example, like thresholds, calibration constants *etc.*, while the global records hold information like drift velocity, status of readout crates (on/off), *etc.*

```
GLOB$DET*
GLOB$DET*.GLOB$SEG1
GLOB$DET*.GLOB$SEG1.SENS$WIRE
GLOB$DET*.GLOB$SEG1.SENS$PADS
GLOB$DET*.GLOB$SEG2
GLOB$DET*.GLOB$SEG2.SENS$WIRE
GLOB$DET*.GLOB$SEG2.SENS$PADS
```

Figure 2.2: The calibration data base structure of a fictional detector.

In CARGO there are five different record types which are identified by a suffix to the record name:

- **B**asic records (**.B**) which is the start of the data base. It is not possible to write update record names that does not exist, or have a date and time of validity that occurred earlier than what is defined in the basic records;
- update records that replaces the earlier record **C**ompletely (**.C**);
- **F**ield update records (**.F**) which should replace (or add) complete data fields in the .B or .C records;
- **W**ord update records (**.W**) which replaces one or more words in an existing field;
- records (**.Z**) to close the validity period of a given module.

Each record holds a number of *fields* that contain the data. The fields available depend on which record they belong to. A list of field names in the `CALB`, `GEOM`, `MATC` and `SCON` trees, which are of more interrest to this thesis, can be found in [15, 16]. In each field the first word is always the number of data words that follow. Continuing the example in figure 2.2 and having ten wires in the sensing device of `SEG1`, the field containing the physical channel numbers of each wire may look like figure 2.3. The values in a field are normally separated by commas, but a *newline* character can also be used for separation. It is also possible to write comments in the data base ASCII file. All comments should be preceded by the character `!`, and any text after such a character is then ignored by the program that imports the ASCII file to the data base.

Accessing the data base can be done either by using one of five CARGO utility programs interactively and/or in batch, or by calling certain FORTRAN subroutines in a program and link it to the CARGO library. The utility programs are:

```
*DBRECORD
CALB GLOB$DET*.GLOB$SEG1.SENS$WIRE.B
890101, 0
*DBFIELD CHAN
10, 1, 2, 3, 4, 5, 6, 7, 8, 9, 10
```

Figure 2.3: The field of physical channel numbers of a fictional detector.

- **DTOBIN** which writes ASCII files to the binary (direct access) data base, *i.e.* it *imports* ASCII files. It can be used both for data base creation and, later, for adding data to an existing data base.

- **DPLOT** which produces *trace plots* of any value in the data base, makes histograms of frequency of data base updates *etc.* The output may be written to PostScript files.

- **DTOBCD** which converts selected binary data to ASCII format for data exchange or visual checking.

- **DLIST** which lists selected contents of the data base directly from the system and/or data files.

- **DEDIT** which deletes records from the data base. Before any record is deleted from a binary data base file it is first automatically exported to an ASCII file.

The data base direct access data files are write protected by passwords, *i.e.* it is not possible to write new data entries into the data base without supplying a password when connecting to it in the user program.

In DELPHI one has to distinguish between the on-line and off-line data bases. The on-line one is updated in real time and the update records are sent to the off-line data base in time for the physics data to be analysed. All detector groups are frequently updating the on-line data base during data taking. Periodically the on-line data base is replaced with a *snap shot* from the off-line data base in order to keep its size low. When doing a snap shot one creates new data base files and supplies a validity date and time. The utility program reads the existing data base and extracts all records and fields valid at this date and writes basic records of these. All records that has a closing validity date and time before the one given for the snap shot are disregarded. This means that the new files start at the timestamp given when doing the snap shot and they contain only the records valid then, and, thus, is a subset of the complete data base.

The off-line data base is usually not updated by a user. In case there is need to update it, an ASCII file containing the update records is created and it is then imported to the data base by one of the data base experts.

The internal structure of the data base inhibits overwriting of existent data. Instead, each data base record has a start of validity date and time stamp, and when importing update records their start of validity is written within the new records. When reading

something from the data base one has to supply the date and time from when the parameters should be valid, and the tools used for reading check this to the validity periods of the records in the data base in order to find the correct parameter values. It is then very easy to correct corrupted values in the data base by writing new records with the same start of validity date and time as the corrupted records have. However, the drawback is that the physical disk size of the data base increases a lot each year.

Apart from the CARGO Management Package there also exists a Detector Description APplication Package [17], **DDAPP**, that was designed to perform the following operations:

- load data from the DELPHI Data Base into an internal memory structure based on the *ZEBRA* package;
- maintain automatic coherence of the data with the date and time given by the user;
- provide the user an access to currently loaded data;
- support tracking through DELPHI geometrical shapes.

This package is used by the analysis programs for reading the data base at an event-by-event basis. Since it uses a ZEBRA structure for storage the speed of reading the data base is increased considerably if the allocated memory is large enough.

2.2 The structure of the VSAT data base

The VSAT part of the DELPHI data base is a set of data records describing the geometrical structure and the sensing device characteristics of the detector. These records are used on-line for quick analysis of the data in preparation for data quality checking, off-line when analyzing the data, and for Monte Carlo simulation of the detector.

For historical reasons the topmost level of the VSAT data base is not called 'VSAT'. Instead the detector is divided into four modules called LUM1, LUM2, LUM3 and LUM4, and each of these have a data base of their own. Luckily, the structures of these four data bases are identical.

Four of the data base trees are used for VSAT to contain all its parameters, the `GEOM` tree has the geometrical constants, `MATC` the materials of the detector, `SLOW` the parameters for the Slow Control system, and `CALB` holds parameters like calibration constants, thresholds, readout channel status *etc.*

A detailed description of all VSAT constants in the `GEOM` and `CALB` trees is given in appendix B. This section gives some complemetary information and describes changes since the DELPHI note was written.

2.2.1 Geometrical constants of the VSAT

To define the exact positions of the VSAT modules it is necessary to do a so called *survey*. This implies that the modules are dismounted from their positions at the LEP beam pipe and high accuracy laser measuring instruments are mounted on their special precision platforms. This is a difficult procedure that takes two days and it is only done when the

modules are about to be placed at or removed from their platforms. The LEP schedule is such that it runs continuously for about six months, and then allows for six months of detector maintenance. The VSAT is dismounted after the end of data taking each year, just before the DELPHI end caps are moved away from the barrel, and remounted some months later, after the end caps have been put back to close DELPHI. Thus, there are two opportunities each year for making surveys.

Out of a survey comes a very long table of numbers that are converted to exact positions of the individual modules. These are then compared to the previous `GEOM` contents of the data base. If there are any differences between the old and new values that exceed the tolerances given by the survey measurement uncertainties, the data base is updated with the new values.

The relative positions between the two modules on the same side of the DELPHI interaction point can be measured to a precision of 0.1 m, while the absolute positions with respect to LEP and DELPHI has a precision of 0.4 mm in x, 1 mm in z, and 0.1 mm in y. The surveys from the last few years show that the positions at the beam pipe are very well replicable within the uncertainties. Thus, the geometrical constants in the database have not been updated since 1991.

As written in section 1.2.9, the VSAT is a sandwich type calorimeter with silicon planes interspaced with tungsten absorbers. The data base contains the dimensions of all these planes, FAD planes, strip planes, tungsten absorbers, and also the gaps between the absorbers and silicon planes. The structure of one module can be seen in figure 2.4.

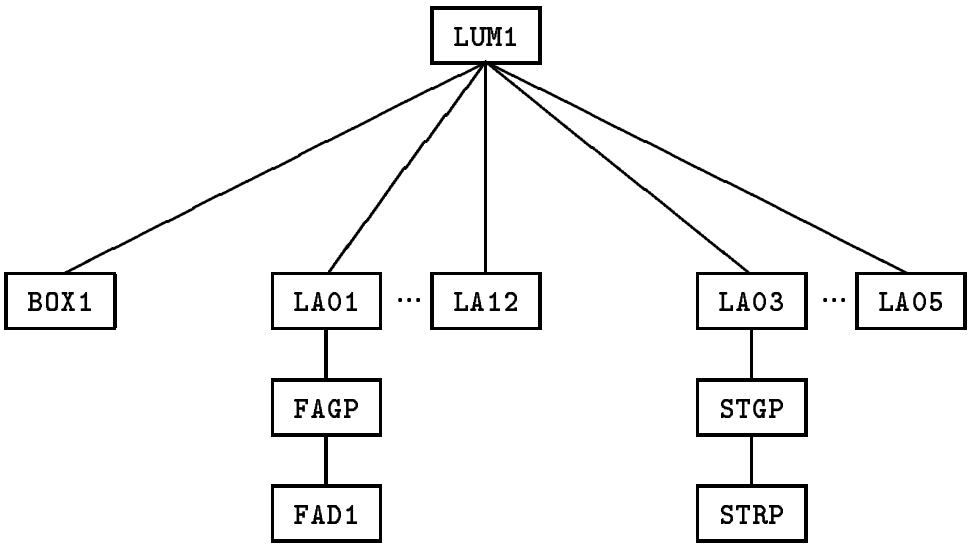

Figure 2.4: The tree-structure of the `GEOM` record set for a VSAT module

The `BOX1` record contains the dimensions of the detector module and its placements with respect to the DELPHI interaction point. For each layer, `LA01` to `LA12` there are three levels of records. The lowest level contains data for the tungsten absorber. The second level, `FAGP`, contains data for the gap between the absorber and silicon planes, the material in this record is air. The last level holds data for the silicon plane. In addition

to these layer records, there are also additional records for the strip planes with the strip gap, STGP, and the silicon strip plane, STRP.

2.2.2 Calibration data base for VSAT

The calibration data base contains parameters, such as voltages, thresholds, calibration constants, channel status *etc.*, necessary for the simulation and/or reconstruction of events in the detector. These parameters may change during data taking, *e.g.* the thresholds and voltages fluctuate slightly all the time, and therefore it was decided to have a software program running on-line to update some of them, see section 2.2.4. The updates made on-line are then sent to the off-line processing farm at each end-of-fill, well in time for the data to be analyzed.

Besides the four trees, LUM1, LUM2, LUM3 and LUM4, the calibration data base also contains a record called LUM*. It is necessary for software programs to connect to all four trees in one function call to be able to update parameters for all four modules, and that can only be done through a common basic level record such as LUM*. This record also holds the status of the data acquisition Fastbus crate and the low voltage bias supply crate as monitored by the Slow Control system. These two crates are common for all four modules and the LUM* record is therefore the logical place to put their status.

Each tree then contains one record for each layer in a detector module, which in turn has sub-levels containing data for the FAD and strip planes, such as bias voltages and currents, channel numbers, thresholds, status *etc.* The structure of a module tree can be seen in figure 2.5.

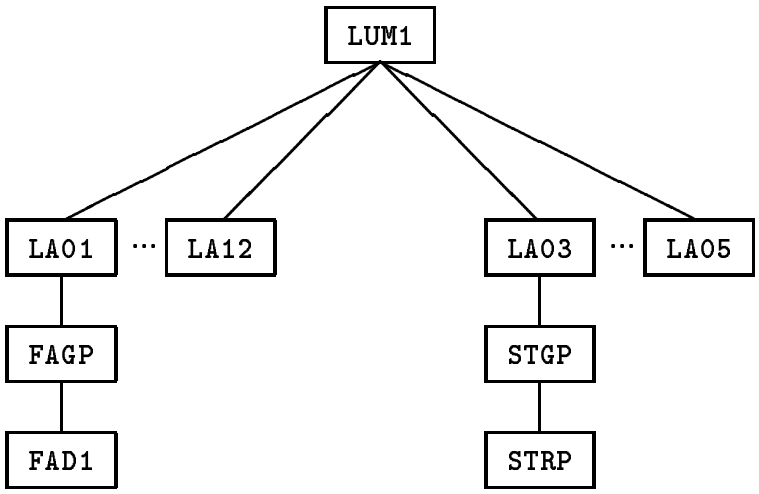

Figure 2.5: The tree-structure of the CALB record set for a VSAT module

There are three levels for each layer, two GLOB and one SENS records. The lowest level record is not used for containing data. In the second level record only the SLOW field is used, it stores the bias voltages and currents for that specific FAD or strip plane. The third level record is the most important one since it holds all channel specific parameters.

Since there is one record per layer, each FAD plane has its own record (containing data for only one channel), while the strip plane records hold data for all strips in a plane, *i.e.* 32 channels in an x-strip plane and 48 in a y-strip plane.

The important data is contained in three fields:

CHAN: contains the physical channel numbers, 1 in a FAD record, 1 through 32 in an x-strip record and 1 through 48 in a y-strip record.

STAT: this field contains the status of each channel and, thus, has as many words as the number of channels for that record. A status of 0 means that the channel is working properly, while status 1 indicates a bad channel.

CALW: this record is slightly different for the FAD and strip records. For each FAD it contains seven values

1. the channel threshold value taken as a mean value from a large number of empty events.
2. The rms width of these empty events threshold values.
3. A second order calibration constant calculated for data taken with a pulse trigger. The value is a mean of several such events.
4. The rms width of these pulser events.
5. A third order calibration constant extracted from data taken triggering on α-particles coming from a source painted on the back of each tungsten absorber. Also here it is a mean value from a large number of events.
6. The rms width of the events from the α-source.
7. Calibration constants evaluated from physics data.

For each strip record there are only five values, the α-source calibration constant and width doesn't exist for the strip planes. However, the other five values exist one for each strip, making a total of 160 words for x-strip planes and 240 words for y-strip planes.

Due to problems with the α-triggers, such as differences in intensity from the individual sources, the third order calibration constants have never been reliable enough to be used. Neither have the second order constants from the pulser data been used for physics analysis. The pulser is only used for confirming that all electronics channels work properly.

2.2.3 Slow Control data base for VSAT

The Slow Controls data base tree (`SLOW`) contains various parameters that are necessary for the Slow Control (SC) system to perform as designed. Its structure is quite complex, as described in [16]. There are some SAT (STIC) and VSAT specific things that are listed here. The BIAS subsystem is very special and required custom designed hardware and software.

As opposed to the GEOM and CALB trees, it contains only one VSAT tree, called VSAT, since all parameters in it are common to all four modules.

In the lowest level record there are three fields:

SPAR: This is a variable length field containing the detector-specific list of SC subsystems. In the VSAT case it is BIAS, the bias voltage monitoring/control system, SWST, the SWitch STatus of the BIAS crate (ON/OFF), and FB**, the monitoring/control of the Fastbus crate.

LISC: A variable length field containing the list of G64[1] crate numbers used in the SC subsytem for a detector. The VSAT shares a G64 crate with the STIC, so this field contains only the number 1.

NAME: A character string describing the root level, *i.e.* the detector name

```
VSAT Very Small Angle Tagger
```

There are three different items of data associated with each subsystem listed in the SPAR field.

Subsystem Description

There is a record containing a text description that indicates what the physical aspect of the detector subsystem name refers to. For the VSAT the records are called:

`SCON$VSAT.DESC$BIAS`	for BIAS subsystem
`SCON$VSAT.DESC$SWST`	for SWST subsystem
`SCON$VSAT.DESC$FB**`	for FB** subsystem

Standard Constants

A set of standard constants that may apply to all the logical channels of this type are stored in a single variable length field of REAL*4 words is one data record for each subsystem. The names of these records are similar to the description records with DESC interchanged with STCO. For the VSAT these fields only contain the real value 1.0 for all subsystems.

Logical Channels Data

To relate logical channel numbers to their physical addresses, one record per subsystem of type LTOP is used. It contains one field which holds a logical-to-physical address correspondence table with 4 integer values for each channel:

1. G64 crate number, always equal to 1 for VSAT.
2. Slot number of the hardware card in the G64 crate, 2 for BIAS, 7 for SWST and 7 and 8 for FB** (slot 7 is for monitoring the Fastbus crate and slot 8 is for controlling it, *i.e.* switching it on or off).

[1] G64 and all other new terms will be explained in chapter 3.

3. Physical channel number on the hardware card.

4. Function flag, which tells the slow controls software what kind of channel it is, *e.g.* flag 1 is a digital monitor channel (SWST and FB**), flag 3 is a digital control channel (FB**), and flag 6 is an analog monitor/control channel (BIAS).

For each logical channel there is one data record required — its type depends on the function flag. For the VSAT BIAS system, this type is ASMD (Analog Setting and Monitoring Data). It has 7 fields:

ANAS: a variable length field for analog setting data with five real words: desired voltage, standard test value, lower limit, upper limit, and precision. The contents in the data base are: 25.0, 0.0, 20.0, 30.0, and 4.0 respectively.

ANAM: a variable length field for analog monitoring data with nine words: desired value, error limit, switch limit, error checking flag (0=NO, 1=YES), gain value, error checking routine in G64, lower limit, upper limit, and precision. The first six words are mandatory but only the first and last three are used for VSAT BIAS.

COMM: a text field containing the description of the channel. This text string is used by the software to identify each channel.

CARI: a field of 4-character words indicating the identifiers in the `CALB` data base tree that should be updated if the monitored value of the channel is outside the tolerance limit given in the `TORA` field. For example, the voltage and current of the first X-strip plane in module LUM4 should be written to record

```
GLOB$LUM4.GLOB$LA03.GLOB$STGP
```

and the contents of the `CARI` field for this plane is

```
LUM4, LA03, STGP, GLOB
```

SCGL: this field is only needed if the list in the `CARI` field contains at least one `GLOB` identifier. It holds the locations in the `SLOW` field of the `GLOB` record(s) which need to be updated. For the above `CARI` field, this field should be

```
*DBFIELD SCGL
3       ! number of words following
2       ! number of locations in  SLOW field
1       ! location of voltage value
2       ! location of current value
```

USER: an optional variable length field containing four real values. All values concern the bias currents. They are: the desired current value, lower limit, upper limit, and precision.

TORA: an optional variable length field that contains two words: the monitoring interval (in seconds) and the tolerance limit on desired value. For the VSAT these values are 600.0 and 1.0 respectively.

For the VSAT SWST subsystem the type of data record is MOND (MONitoring Data) and it contains 5 fields:

DIGM: a variable length field for state-monitoring data with the three first words defined as: desired state (0=OFF, 1=ON), error checking flag (0=NO, 1=YES), and error routine number in G64. For VSAT the values in the data base are: 1, 1, 0.

COMM: same as for the `ASMD` record.

CARI: same as for the `ASMD` record.

SCGL: same as for the `ASMD` record.

TORA: same as for the `ASMD` record.

Finally, for the VSAT FB** subsystem there are two types of data records. One is the MOND described above, and the other is the SETD (Setting Data) record, which contains two fields:

DIGS: a variable length field with the two first words defined as: the desired state and a standard test state. Both are integer values and restricted to values 0 (=OFF) and 1 (=ON). Both values in the VSAT data base are set to 1.

COMM: same as for the `ASMD` record.

The `SLOW` tree of the data base is read by the slow controls software programs which make use of the parameters defined in the data base to configure the hardware and to decide the slow controls state. All these programs are described later in chapter 3.

2.2.4 On-Line Data Base updating program package (ODB)

In the beginning of 1991, it was decided within the VSAT group that some parameters such as status, thresholds and calibration constants of individual read-out channels should be updated to the data base on on-line basis. Therefore, a FORTRAN program was needed for taking care of this, and what came out was the *ODB* program package.

At first, the intention was to write only one program that takes care of the on-line updating, but while writing the source code for it, two other useful programs evolved. Their functions are all described below, and there exists also a manual [19] that goes much more into details about the programs, their structures, and formats of input and output files.

There is a lot of source code that is common for all programs and all this is collected into a library file, which is then used when linking the special application code into an executable program file.

ODBUPDATE program

This program runs continuously in the `USER_CONTROL` batch queue on the VSAT on-line data acquisition VAXstation, *WSDEVS*. It is normally in a hibernating state, *i.e.* it is doing nothing at all but waiting for a wake-up call from another process.

At every end-of-run, the VSAT on-line data monitoring program writes some files containing status of read-out channels, threshold values of these *etc.*, derived from the

data acquired during the run. It then sends a wake-up signal to ODBUDPATE, which reads the same files, compares the new values with what already is written in the data base, and, if the new values are outside specific tolerances defined in ODBUPDATE, it writes update records directly to the on-line data base. After all this is done, it goes back into hibernating, waiting for the next wake-up call to come.

Originally, the program was written to take care of four things: status, threshold, and calibration of each read-out channel, and the energy correlation constants which are used for translating read out energy ADC counts into GeV. However, the calibration constants were calculated using an iterative method and could therefore not be extracted on-line. Also, the calculation of energy correlation factors was not reliably done on-line. As a result, flags were put into the ODBUPDATE program to enable/disable the handling of these two data base parameters, and they have always been disabled.

The ODBUPDATE program has run for several years without any major problems. It has showed a good reliability and has been very useful.

ODBREAD program

It is quite important to be able to see directly the contents of the data base when developing a program that updates it. Using the DLIST program is quite easy as well, but it assumes some prior knowledge of the data base structure in order to find whatever one is looking for. The ODBREAD program was originally created to allow easy access to the contents of the data base, without any such prior knowledge.

The program needs two logical variables defined. The first is a word that tells the program what it should look for, *e.g.* `STATUS` for looking at read-out channel status, `PEDESTAL` to look for channel thresholds, *etc.* The second argument is the date and time for which the read values should be valid. It is read as a character string with the format `date.time`. The results of a data base search are written to the screen and to an output file.

ODBCALW program

This program is basically a short version of ODBUPDATE. As with ODBREAD, it needs two defined logical variables. The first is a word describing what the program should update, similar to the first variable of ODBREAD. The second is a word telling the program whether or not it should compare its input values with what is already in the data base before the update is made.

The ODBCALW program does not hibernate waiting for a wake-up like ODBUPDATE. It runs through the updating code only once and then exits with a status result showing whether it was successful or not.

The option to write updates without first comparing them to the existing values in the data base has proved useful to correct corruptions in the data base. These corruptions have appeared when test runs of the VSAT data acquisition system were made, and both the on-line monitoring program and ODBUPDATE were running, but without BIAS voltages connected to the silicon planes. All parameters calculated by the monitor will then be completely wrong, and differ enough from the values in the data base to be written as updates.

Chapter 3

Slow Controls System

The Slow Controls system is responsible for monitoring and, in some cases, controlling various things such as high- and low voltages for various sub-detectors, switch status of individual electronics crates, temperatures inside the detector *etc.* While the data acquisition system must have very short response times, in the order of μs, the slow controls system has much longer response times, $\approx$ minutes.

It is a complex system of many programs running on different computer platforms, and communicating with each other over ethernet using TCP/IP. This chapter describes the DELPHI slow controls system in general and the VSAT and STIC systems in more detail. Some parts of the STIC slow controls were inherited from the old SAT system, but there are a few new objects, *e.g.* high voltage system for the read-out tetrodes. For the STIC, only parts in which I was personally involved are touch upon here.

3.1 DELPHI Slow Controls System

The DELPHI detector has been equipped with an automated system for monitoring and controlling technical aspects of the experiment, such as high and low voltages and gas supplies, for reporting and acting on changes in the status of the detector or its environment, and for maintaining the safety of the equipment. This system is known as the *Slow Controls* [20]. The overall structure of the system can be seen in figure 3.1.

The DELPHI Slow Control system is highly modular and highly distributed with many programs running on both high-level (VAX) and front-end (G64) processors. A DELPHI slow controls operator makes use of two main graphical displays, shown in VAXstation windows. The status display gives a color-coded representation of the states of the the various detectors. These states are defined in the *State Management Interface* (SMI) which is a hierarchial set of objects representing different aspects of the detectors seen by the slow controls system. SMI is also responsible for passing commands down to the appropriate subsystems. The other display is the error message display which shows outstanding anomalies in textual form. These messages are handled by the *Error Message Utility* (EMU).

Both SMI and EMU show conditions determined by the *Elementary Processes* (EP), which are the lowest level VAX control programs. The EP's are also responsible for handling SMI commands, logging state changes to the data base for use by the off-line

analysis, and providing a route for occasional expert intervention, using a user interface, *HIPE*.

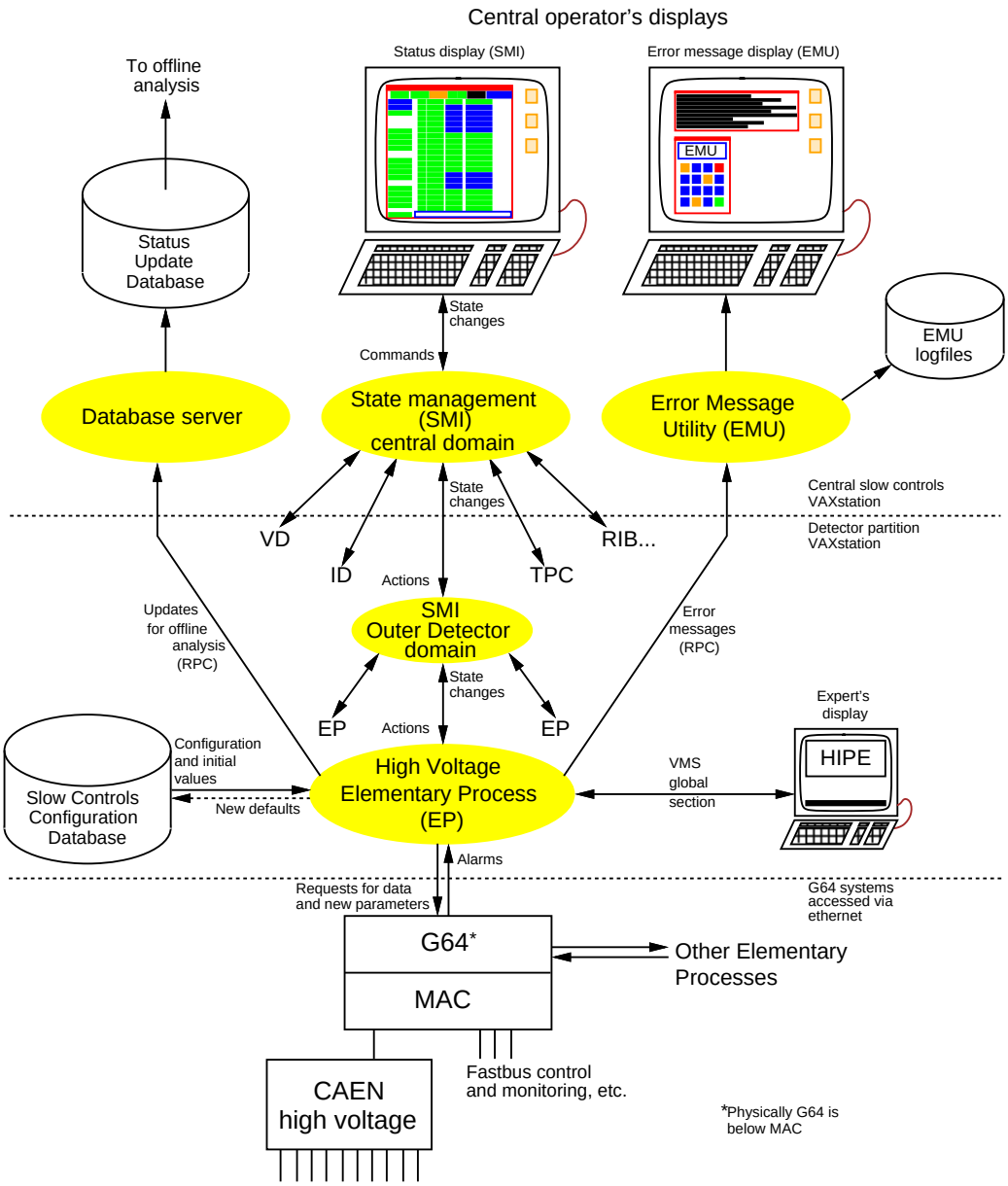

Figure 3.1: Diagram of the overall structure of DELPHI slow controls system represented by the example of the high voltage control of the Outer Detector.

With the use of the *Remote Procedure Call* (RPC) protocol, the EP's communicate over ethernet with the front-end control and monitoring micro-computers, the *G64* crates. The G64s monitor and control a variety of different types of hardware using digital and analog devices.

The unified *gas system*, which controls and monitors the flows and mixtures of gases supplied to various parts of the detector, and the *GSS* safety system, which monitors the detector and its environment for hazardous conditions, use different structures, but are

integrated with the rest of the slow controls at the SMI and EMU level. These software links are complemented by a system of hardwired interlocks.

3.1.1 Front-end Systems (G64)

The G64 systems are the lowest level of computer functionality. They are located in the electronics counting rooms adjacent to the detector in the experimental cavern. The number of G64s used by each sub-detector depends partly on the fact that their electronics may be spread out to more than one counting room, and partly on the complexity of their individual electronics systems and multitude of sub-systems, such as temperature probes, high-, low- and drift voltages, *etc*, that needs to be montiored and/or controlled remotely.

G64 Hardware

G64 is a simple 64-line microprocessor bus developed by the Gespac company. Its simplicity has led to the production of a number of cheap input/output cards, and it is, thus, well suited to an experiment with a requirement to monitor and control a very large number of channels, without any particular emphasis on speed.

The G64 crate, *MAC-G64*, was designed by CERN ECP division. It contains two card frames, the lower has a G64 bus, and the upper is used for holding the *MAC* (monitoring and control) cards. These cards have specific input or output functions, *e.g.* multiplexing analog signals, and are read out using a small selection of G64 cards, *e.g.* analog-to-digital converters, digital input/output cards *etc*, in the lower card frame. This separation enables a small number of cards to be used for a variety of functions, simplifying the software and the maintenance of the hardware. It also reduces noise problems by allowing the MAC cards to be separately grounded.

The CPU card used by DELPHI consists of the Motorola 6809E microprocessor, 56 kilobytes of RAM, 32 kilobytes of ROM, two serial RS232-C interfaces and a real-time clock. Peripherals on the G64 bus are memory-mapped into a 1-kilobyte region, the *Valid Peripheral Address* space, which is decoded on the CPU card. Since the 6809 has a 16-bit address bus, it can only directly address a maximum of 64 kilobytes. Additional memory can be addressed by using a paging facility on the CPU card, which allows different 32-kilobyte sections of memory to be brought into use under program control.

Communications with the VAX system is done through a G64-ethernet interface. This contains a 68000 processor, onboard RAM and EPROM, and the LANCE ethernet chip. The G64 CPU has access to a window of the 68000's RAM, and the 68000 can access all of the 6809's address space, allowing DMA transfers.

The main input/output G64 cards used are a Parallel Input Adapter (PIA) card for reading digital statuses, analog-to-digital converter (ADC) cards for reading analog voltage levels, and an Output Register card to control digital statuses. Many of the required ranges accepted by the G64 input cards, or voltages produced by the output cards, are not suitable for direct connection to the detector. The conversion is performed by the MAC cards, input adapters, relay cards, platinum resistance thermometer (PT100) temperature adapter cards, *etc*. The type of each MAC card can be read out by a special G64 card, allowing a cross-check between program configuration and the actual hardware installed.

G64 Software

The G64 contains no facility for multitasking. The 4-kilobyte monitor program in EPROM handles the initialization and provides basic routines for terminal and disk input and output. When the system is switched on or reset, the monitor either bootstraps the operating system from disk or loads the application program from EPROM. The *FLEX* operating system allows the editing, compilation, and running of programs from disk. The startup procedure from EPROM is much faster than from disk, but it is easier to change programs on disk, so in the development phase the program should be loaded from disk, whereas when the program is stable it ought to be put in EPROM.

Most application programs for the G64 have been written in Omegasoft Pascal. In addition to standard Pascal features, this compiler allows the program to be split in separate modules, and allows direct addressing of memory-mapped peripherals. The size of the standard DELPHI application program is larger than the 64-kilobyte address space can hold. A mechanism has been developed to allow different modules of a program to be placed on different pages in memory, overcoming this problem.

Communications between the VAX and G64 systems use the OSI transport protocol over ethernet. The protocols are running on the G64-ethernet card. An interface to this, CATS/TP4, has been implemented on the G64-ethernet card, using the CATS (common access to transport service) calling standard developed at CERN. CATS attempts to standardize calling sequences to different transport protocols and implementations. A simple protocol allows CATS calls on the G64 to be executed on the G64-ethernet card using the shared-memory window.

Remote Procedure Calls (RPC) are used both on VAX and G64 to communicate commands and data. RPC is based on a client-server model, and allows network calls, *i.e.* calls to CATS, to be hidden from the application. The client application calls an application-defined routine which is implemented on the server. The RPC system takes care of transmitting the request, along with arguments, to the server. The server RPC system then calls the requested routine with the arguments decoded from the received message, and, after its completion, sends back the return arguments to the client RPC system, which returns them to the client application.

The G64 application program executes a continuous loop, monitoring all input channels. Any status change is flagged by calling a reporting routine on the VAX via RPC. For the sake of efficiency, if the G64 detects several status changes within one monitoring loop, up to ten of these are buffered into a single RPC call.

3.1.2 VAX Systems

The VAX systems used in the slow control system are located in the surface control room, where they are connected to the various G64 processors via ethernet. Each major detector partition has one or two VAXstations, which perform local data acquisition, monitoring and slow controls. In addition, there is also a VAX 4000 for the central slow control.

The VAXstations run under the VMS operating system, which provides multitasking, virtual memory, a networked filestore and a large set of system routines. The slow controls software has made heavy use of event flags, mailboxes, interrupts (VMS ASTs), global sections and logical name translation services [21].

Elementary Process (EP)

The *Elementary Processes* (EP) run in the detector partitions' VAXstations, and are responsible for the communication with the G64s. The EPs consist of a standard skeleton program with a set of user routines in which each detector group add code to handle non-standard subsystems, *e.g.* the STIC and VSAT bias subsystem.

Each elementary process handles one subsystem of a detector partition, and is represented in the SMI by a single object whose state indicates the condition of that subsystem. The EP is essentially the link between the G64s on one hand, and the State Management Interface (SMI), the Error Message Utility (EMU) and the expert user interface HIPE, on the other. It is also responsible for updating the status data base. In order to handle interrupts from many of these sources, as well as to perform periodic monitoring, it is by necessity event driven, using the mechanism of VMS event flags.

Channel definitions, normal settings, and conversion factors are read from the slow controls data base. This also defines the names for each channel in order to make any error messages to EMU helpful for the operator. The overall program configuration is defined by VMS logical names.

The elementary process can accept commands from, and report state changes to, SMI. At any given time a single SMI state is evaluated to represent the status of all channels overseen by an EP. SMI commands perform actions such as switching apparatus on, off or to an intermediate level.

Each elementary process communicates with one or more G64s, and each G64 can handle up to eight EPs. Status change reports call an RPC routine as an interrupt (VMS AST level), allowing immediate timestamping and reporting to EMU. Other actions, such as recomputing the SMI state, are queued for subsequent execution. State changes in each channel, reported by the G64, are sent to EMU. These generally indicate an error condition being either raised or cancelled.

Changes in channel statuses and in parameter values determined by periodic monitoring of the hardware are written to the status data base for use by the off-line analysis. Data base updates are usually inhibited when no data is being taken in order to minimize the number of updates due to the raising and lowering of high voltages at the start and end of data-taking.

State Management Interface (SMI)

The *State Management Interface* (SMI) shows the status of various subsystems of the experiment by a set of *objects*. Each object has a predefined set of states which it can obtain, and each state has a set of actions that can be requested for it.

The objects are linked together starting with a layer of elementary objects, each representing the states of a subsystem monitored by an elementary process. These objects are linked together to a sub-detector object that show the overall state of all elementary objects of that detector. The sub-detector objects are then linked together to a central object that shows the overall DELPHI status, see figure 3.2. Actions requested of an object are either passed on to other objects at a lower level or, by the elementary objects, to an elementary process.

The definitions of possible states, allowed actions, and the relationship between objects

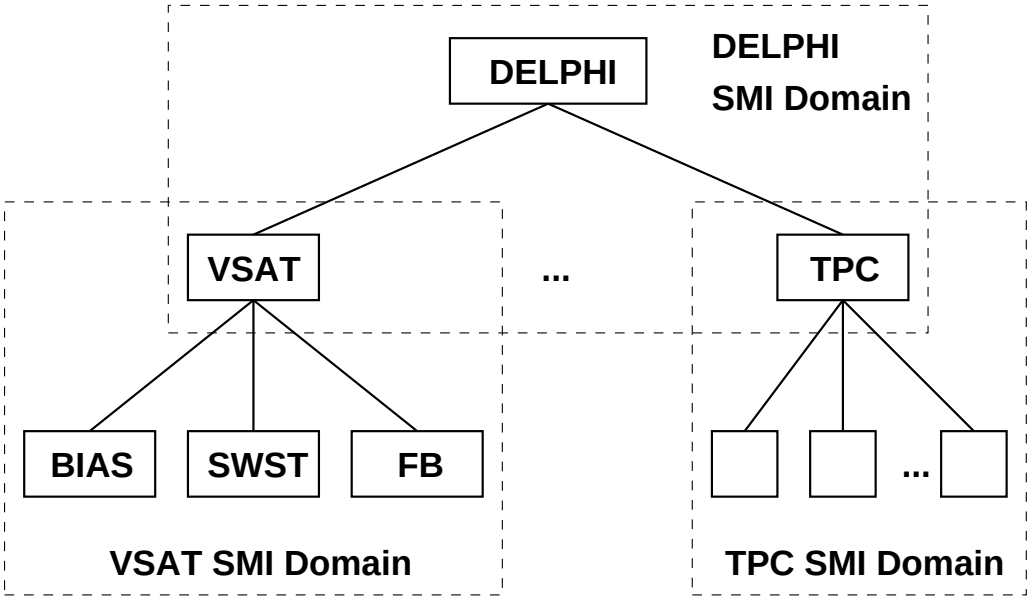

Figure 3.2: The SMI hierarchy of DELPHI.

is made in a dedicated SMI language, SML. For the non-elementary objects, SML allows logical conditions to be specified which will result in an automatic state change or set of actions. For example, the state of a higher-level object is determined by the states of lower-level objects, or commands can be issued when a state change occurs.

A group of related objects forms an *SMI domain*, which is implemented in a single process. For example, in figure 3.2 the elementary objects BIAS, SWST and FB form a domain together with their 'parent' object VSAT. Also the objects from VSAT through TPC, including all other subdetectors, form a domain together with the 'parent' object DELPHI.

Expert Interaction (HIPE)

The SMI allows display and control of entire subsystems, *i.e.* clusters of channels in an elementary process. It may, however, be desirable to be able to display or control individual channels in one such subsystem. This is effected using the *HIPE user interface*. This allows, for example, high voltages to be adjusted for problem channels. At a command from HIPE, these modified values can then be written by the elementary process to the slow controls data base, to become the new standard values. HIPE uses a VMS global section to retrieve information directly from the EP's datastructures in memory. This keeps interactive access from interrupting the work of the elementary process.

HIPE user interaction is based on the MHI menu package. The definitions of the elementary processes to which HIPE must connect, the channels and groupings, and the menu structure is made in a configuration file.

The HIPE user interface is a powerful tool when it comes to tracing error and/or problem conditions down to their origin, *e.g.* temperature read-out channels out of range. As mentioned before, it is also useful for adjusting the settings of individual channels.

Error Message Handling (EMU)

The Error Message Utility (EMU) is a CERN product which provides a unified system for handling alarm, error, warning, and informational messages from the slow controls and data acquisition systems. Messages, which can be sent from anywhere on the network, are formatted by the EMU system according to a message description file. They are then sent to one of a number of logfiles or destination processes according to a message routing file.

The application programs connected to the EMU system inject their messages into EMU using a message name, *e.g.* `set_error` or `clear_error`, and usually some parameters such as the channel name, newly-read value *etc.*

Each sub-detector has one EMU logfile which is normally only of interest to the detector experts. All messages from that detector, or relevant to it, are also sent into central logfiles, one for slow controls and one for data acquisition, which are watched by EMU displays on the central VAXstations. New versions of the logfiles are created at every midnight, while the old versions are kept for inspection by detector experts.

EMU messages corresponding to conditions that require rapid intervention from a detector expert are routed to a *beep-caller* program which makes use of an auto-dial facility of a modem to dial the telephone number to activate the pager carried by the appropriate detector expert.

3.1.3 Ancillary Systems

So far, only systems that monitor and control the technical aspects of the detectors have been described. There is a number of ancillary systems that have been developed independently of the detector slow controls system, but were interfaced with the DELPHI slow controls at the EMU and SMI levels to allow the operator easy access to the conditions of these systems, and to allow for automatic actions in serious situations.

For the completeness of the DELPHI slow controls, these ancillary systems will be briefly described below.

Gas Systems

The gas system was developed within the DELPHI collaboration and use a combination of G64 and VAX computers. Here, much more intelligence is vested in the G64s, while the VAX is used only for user interaction, logging, and interfacing with other systems. This allows the gas system to operate independently of the VAX computers, and run outside normal datataking periods when the other systems may be subject to frequent downtime. The disadvantage is that it has lead to comparatively inflexible systems as program development on the G64 is painful, and the program size is limited.

All detector gases are provided by an integrated system of supplies, mixers, distributors, and purifiers, the state of which are controlled by 28 G64 systems. Another six G64s act as supervisors, and are equipped with graphical displays and can control equipment and show the results of measurements throughout the system. Flow rates and compositions are carefully monitored, as anomalies could indicate a gas loss or a dangerous mixture.

Serious conditions are sent to a server on the VAX, which can raise an SMI ALARM state for the parts of the detector affected. An EMU message describing the problem for the operator is then also injected. The ALARM state causes the high voltages of the detector to be ramped down, and provides a backup to a hardwired connection directly from the gas system to the CAEN high voltage units.

General Surveillance System (GSS)

The safe environment of all four LEP experiments, as well as LEP itself, is monitored independently by the *General Surveillance System* (GSS). It monitors the ventilation, cooling water, temperatures, and flammable gas and smoke detectors. If any problems are detected, it can alert the operator and/or the fire brigade. In addition to this, it can also switch off gas supplies, high voltages, or mains power, and activate fire extinguishers.

GSS is linked to the DELPHI slow controls system by both hardwired signals and computer messages. In addition to this, there is a graphical interface which shows all areas of the detector, and any problems by coloring the parts in question, and if a serious condition arises, beeps continuously to alert the operator.

The hardwired signals are generated in case a serious condition is detected, and are used for switching apparatus off independently of any decision made by the software system. Conditions relevant to DELPHI that are detected by GSS, are sent to a server process on the DELPHI VAX cluster, which translates them into EMU messages and maintains the state of SMI objects for each detector partition and electronics barrack. The SMI state changes can trigger automatic actions such as switching off high voltages, before the condition becomes serious enough to force a hardwired switch-off.

Serious conditions detected within DELPHI, *e.g.* a gas loss detected by the gas system, are forwarded from EMU to GSS, and this allows GSS to take independent action, such as a hardwired switch-off of the gas supplies and high voltages.

Solenoidal Magnet

Like the gas system, the *Solenoid control system* was developed within the DELPHI collaboration, and it also uses G64 and VAX computers with most of the intelligence put in the G64.

The solenoidal magnet uses a superconducting coil carrying a current of 5000 A, maintained at a temperature of 4.5 K. Monitoring is required for the temperature, pressure in the cryostat, current, mechanical strain, and magnetic field in a number of places round the coil. Detailed computer control of the power supplies is also required.

For this four G64 systems are used together with a standalone VAXstation 4000-VLC which provides user interfaces and logs the time-variation of monitored values onto an independent data base.

Anomalous conditions detected by the G64 systems are sent to an alarm server of the VAX. Some of these conditions can provoke automatic actions, *e.g.* ramping down the magnet currents. All messages are injected into a local EMU system which forwards the more serious ones to the main cluster.

LEP Accelerator

LEP sends signals to the four experiments indicating in which state it is, *e.g.* setting up with beam, accelerating, physics, *etc.* These signals are used by the DELPHI slow controls to take appropriate actions for the system. For instance, a physics signal will automatically ramp up all high voltages and make the detector ready for data-taking. Another example is that high background conditions may force DELPHI to ramp down the voltages of sensitive detectors, or, if the conditions are severe, force LEP to dump the beam. After a LEP fill has ended, the signal received from LEP causes the DELPHI slow controls to ramp down voltages to stand-by values and switch off the data base updating facility.

3.2 VSAT Slow Controls System

The VSAT Slow Controls system is in comparison with all other subdetectors quite simple. It contains only three elementary objects, BIAS for the silicon bias supply system, SWST for the switch status of electronics crates, and FB for the status of the read-out Fastbus crate. The implementation of the different DELPHI programs is described in appendix C, and this section contains more detailed information about the objects in the system.

The complexity of the system lies in the BIAS system. This was designed by members of the SAT collaboration [22] for use in the SAT tracker system, and later on adapted to the VSAT silicon read-out planes.

To handle the BIAS system, the standard DELPHI software had to be altered both at the G64 and VAX levels. Also, non-standard G64 MAC cards had to be made for the communication with the microprocessor controlled bias power supplies via RS232.

It is possible to make the elementary processes (EP) monitor the hardware status periodically. The monitor rate is specified in the slow controls data base, see section 2.2.3. When the EP is requested to monitor, it send an interrupt to the G64 that reads the hardware and returns the results to the requesting EP.

3.2.1 BIAS system

Each VSAT module contains 12 full area silicon plane detectors that are powered by a 25 V negative bias. The front plane of each module is connected to a bias supply of its own, while the subsequent planes are connected to the same supply. The reason for connecting the front plane independently was an unknown risk that this plane may take a lot of radiation damage from low-energetic photons coming from the beam, and it would be easy to unplug the cable for this plane should it be necessary.

Apart from the full area detectors, each module also has three silicon strip plane for position measurements which are powered by a 25 V positive bias. These planes are connected to one bias supply each for easy adjustments of bias voltage independently of each other.

All the bias supply units, a total of 20, are placed in one microprocessor controlled power crate, which is connected to the G64 system by RS232. The crate itself can be in three different modes: *LOCAL* which leaves the mains power on at all time, *OFF* which

is the opposite to LOCAL, and *REMOTE* which allows the G64 to control the mains power of the crate. In addition to the RS232 connection, there is a cable between G64 and the crate which handles the remote control of the mains, provided that the crate is in REMOTE mode.

If a periodic monitoring of the bias voltages indicates that a channel differs from the nominal value by more than an error limit defined in the slow controls data base, the elementary process will write an update record to the status data base containing the new value.

3.2.2 SWST system

There are two VSAT modules on each side of the DELPHI interaction point, called forward and backward side modules. The read-out signals from the modules enter a set of multipexing cards that process them before sending them to the read-out modules in the fastbus crate. The multiplexors are contained in two euro-standard crates, one for the forward modules, and one for the backward. In each crate there is a microprocessor card, based on the 68HC11 processor [23], that controls various parameters of the modules, *e.g.* threshold settings, number of planes in trigger, *etc.*

Through these microprocessor cards it is possible to monitor the mains power of the crates containing the multiplexors. Even though it would be seen immediately in the data distributions whether one or both crates were off, it is still valuable to see it in the slow controls as an additional information.

The power status of the multiplexor crates is included in the SWitch STatus (SWST) object, with two digital monitoring channel, one per crate. In addition to this, the power status of the bias crate is also included in SWST, giving a total of three channels.

Whenever one or more channel(s) is not in the desired state, the SWST object will show an *ERROR* state that is forwarded to the overall VSAT SMI object. Also an EMU message will be sent indicating which crate(s) is OFF, and a specific word in the status data base will be set to inform the off-line analysis program that the VSAT is out-of-order.

3.2.3 FB System

The read-out electronics for all subdetectors of DELPHI are contained in fastbus crates. Most partitions have a large number of crates containing *e.g.* shapers, digitizers *etc.* It can then be hard to physically locate the position of a specific crate that is off. To facilitate this it was decided to monitor and control every fastbus crate that are crucial to data-taking.

The fastbus crates were already prepared for remote monitoring and controlling by use of a connector on their front panels. The implementation of fastbus control was then straight forward by adding a digital output card in the G64 setup.

The VSAT FB system contains two channels, one is for monitoring the power state of the crate, and the second is for switching the crate on or off remotely.

If the FB elementary process reads a state change in the fastbus power, it changes its SMI state to *ERROR* and sends an EMU message describing the change and indicating the physical location of the crate. It is then possible to switch the crate back to the

previous state by issuing an SMI command, or, with the use of the location description, go down to the counting room and switch it on by hand.

3.2.4 GSS Systems

Apart from the three elementary objects of VSAT described above, there are also two additional objects that have to do with the General Surveillance System.

The domain GSS has an object corresponding to each DELPHI sub-detector (VD, ID, VSAT, *etc*), and an object corresponding to each counting room (A1, B1, *etc*). The detector objects are set to an ALARM state if there is a dangerous situation in or near the actual detector, *i.e.* in the barrel or end-caps of DELPHI. This can happen if gas losses, smoke, or fire is detected. If the alarm is raised for a detector, its high and low voltages should be switched off immediately, and this can be done in the SMI code.

The same type of logic applies to the counting room objects if a dangerous situation develops there. In this case, the crates containing the read-out electronics should be switched off if possible, *e.g.* all fastbus crates.

The GSS objects are implemented on the SMI level only, where the logic is set so that the correct action is taken. When a GSS alarm state is cleared, the SMI goes into a state called *AL_CANCEL* and this has to be cleared before any apparatus can be switched on again. The reason for the intermediate AL_CANCEL state is that for some sub-detectors, experts have to be called in to reset equipment, *e.g.* power supplies, by hand. For the VSAT detector there is no need of manual intervention after the an alarm has been cancelled, and a clearing of the AL_CANCEL state sets the state determined by the SMI logic based on the three elementary objects.

3.2.5 SMI States, Actions and Recoveries

The three different elementary objects can enter different states predefined in the elementary process. Each state has a number of actions defined in the SMI logics. For any state that appears due to an error of some kind there is a well defined error recovery sequence to be followed by the central operator on shift. If the error persists after this has been done, the instructions are to call in the detector experts who then have to solve the problems.

Table 3.1 shows the possible SMI states that the different elementary objects can enter, and what conditions generate these states. Table 3.2 shows the different SMI commands that can be given, and what actions they correspond to.

Table 3.1: SMI states of the elementary objects defined in the VSAT SMI logics.

SMI state	Condition
DEAD	The elementary process is not running.
ERROR	At least one channel is out of range.
NO_CONTROL	Communication with the G64 has been broken.
NOT_READY	Some channels are on and some are off.
OFF	All channels are off.
ON	All channels are on.

Table 3.2: SMI commands of the elementary objects defined in the VSAT SMI logics.

SMI Command	Action
ABORTIT	Stops the elementary process.
MONITOR	Reads the hardware status.
START	All channels are switched on.
STOP	All channels are switched off.

Apart from the objects connected to the three elementary processes and the GSS, there are two more objects in the VSAT SMI Domain. One is called *CL*, which stands for *CENTRAL/LOCAL*. This indicates if the VSAT slow controls system are under central or local control. Under normal running conditions all sub-detector slow controls should be under central control, allowing the operator to send appropriate commands to all sub-detectors simultaneously. The local control mode is reserved for when, outside of data-taking, intervention is needed for a sub-detector, and thus inhibits the central operator from taking any actions with the system of that partition.

The last objects is called *SC* and it shows the overall state of the sub-detector slow controls system. It has its own set of states and commands defined, table 3.3 for states and table 3.4 for commands. Each state has a number of logical expressions defining state changes of the SC objects if certain criteria should be fulfilled, *e.g.* if any of the GSS objects goes into ALARM, the SC object immediately goes into ALARM as well.

Table 3.3: SMI states of the VSAT SC object defined in the SMI logics.

SMI state	Condition
AL	Unsafe condition, GSS in alarm.
AL_CANCEL	A previous alarm condition, now gone, needs explicit clearing.
DEAD	The local SMI process is not running.
EP_DEAD	One or more elementary processes are not running.
ERROR	One or more elementary objects are in ERROR.
NO_CONTROL	No communication with the G64.
NOT_READY	One or more subsystems is not ready to take data.
READY	All subsystems are ready for data-taking.

Table 3.4: SMI commands of the VSAT SC object defined in the SMI logics. Commands that start with the prefix **C_** are sent from the central SMI. Other commands are local.

SMI Command	Action
C_CLEAR_CANCELLED_ALARMS	Clear a previous alarm condition.
C_PREPARE_FOR_RUN	Switch on all channels not already on.
C_SWITCH_ON_FASTBUS	Switch on fastbus crates.
START_FB	Switch on fastbus crates.
STOP_FB	Switch off fastbus crates.
SWITCH_OFF	Ramp down bias voltages.
SWITCH_ON	Ramp up bias voltages.

As seen in table 3.1, there are a total of six states defined for the elementary objects. Five of them indicate problems with the slow controls system. How to solve these problems is quite easily understood when looking at the conditions for these states. Here is, however, a complementary list on how to recover from different problems.

DEAD: Restart the elementary process that is not running.

ERROR: Here are different procedures depending on which object is in error: BIAS — ramp up the bias voltages; FB — switch on the fastbus crate; SWST — check which crate is off, and switch it on by hand in the counting room.

NO_CONTROL: Reset the G64 crate and run an init procedure that loads necessary parameters to the G64 program.

NOT_READY: Switch on the channels that are not already on.

OFF: Same as for the `ERROR` state.

3.2.6 Radiation Damage to the VSAT detector

Radiation damage has, in a way, a connection to the slow controls system, *i.e.* the bias currents of the detector is monitored by the slow controls, and providing the currents are reasonably stable, it is possible to enter some kind of radiation alarm state if the currents should increase dramatically. This state could then either alert the central operator or, by hardwire, dump the LEP beams.

In the early days of running, the currents were watched closely for indication of radiation damage, especially the currents of the front planes. However, the bias currents showed good stability with no significant rise at all, and the watching slackened.

On September 15, 1995, there was a radiation accident in DELPHI. At 5:30pm injection of electrons into LEP was started, but the collimators, which normally protect DELPHI from radiation during injection, were wide open. This led to a radiation alarm in the DELPHI cavern on the backward side of DELPHI, *i.e.* on the side where the electrons are entering the DELPHI detector. This alarm should have triggered a beam dump, but due to a malfunction no automatic action was taken. There was no sign of high radiation in the center of DELPHI where the internal radiation monitors are placed. Therefore, no feedback on the extremely high background conditions were reported to the LEP control room, and therefore the injection continued.

A lot of the DELPHI sub-detectors, positioned far away from the center, reported high background conditions. The estimated flux of particles in these areas was less than 10^6 particles per second over an area of 50m^2.

The beam was lost around 6:15pm and things went back to normal. However, the event was discussed at length within the collaboration for another few days. It seemed at first that all sub-detectors had survived the incident without any serious damage. There had not even been any sign of high radiation in the center of DELPHI.

Some weeks later it was discovered that the bias currents drawn by the full area silicon planes on the backward VSAT modules had increased by a factor 4. An investigation

started and by the use of the data base DPLOT utility program, see 2.1, it was possible to graphically show that the dramatic increase in the bias current for the two modules started at the date and time of the radiation incident, see figure 3.3. It can be seen in the figure that slightly after 6:00pm on September 15, the current increased from $\approx 11\mu$A to $\approx 42\mu$A. The conclusion was that the VSAT modules were involuntarily used as a radiation shield for the inner sub-detectors of DELPHI, when the beam in LEP was lost.

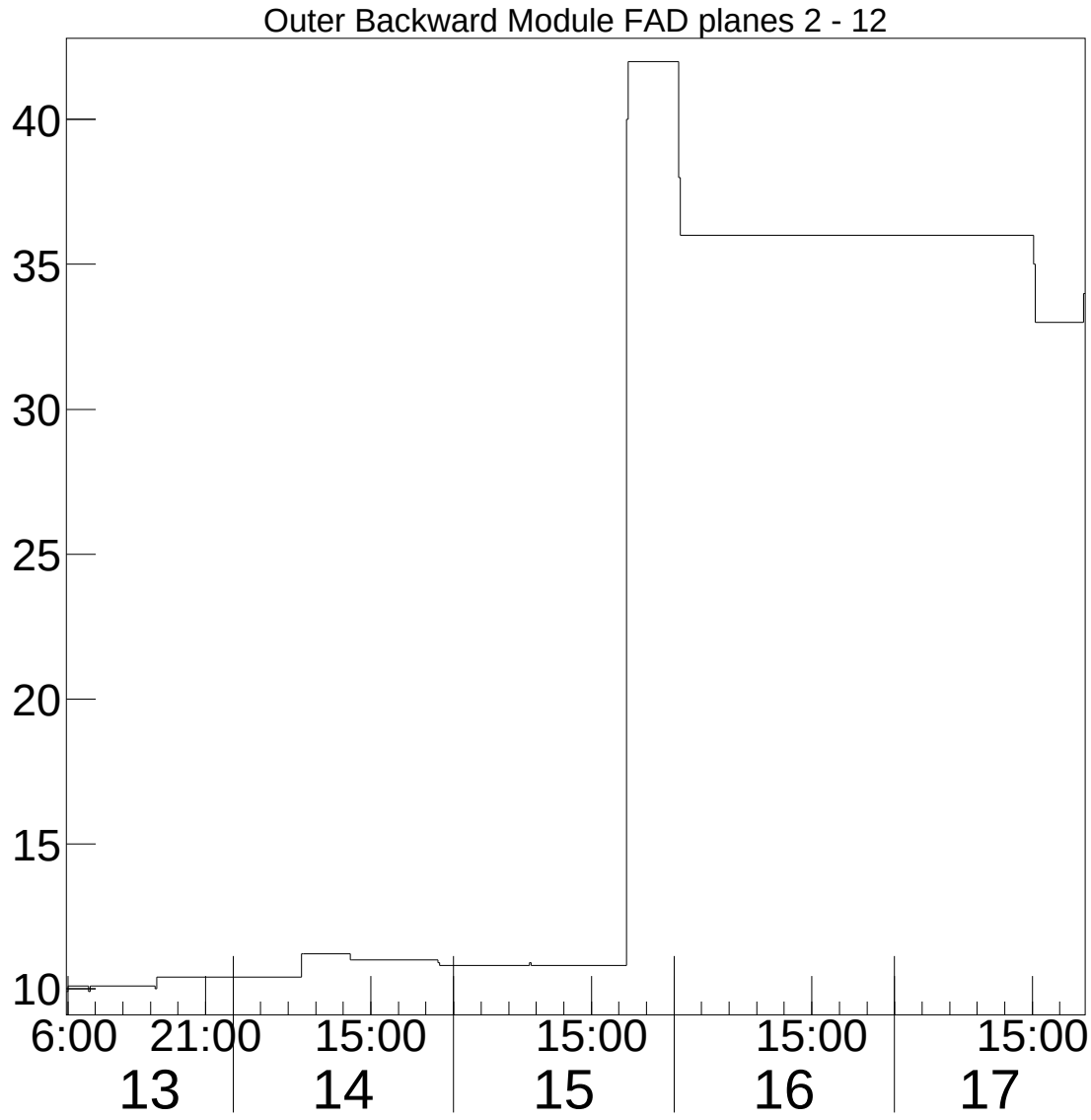

Figure 3.3: The bias currents drawn by planes 2 to 12 of the outer backward VSAT module. Unit on the y-axis is μA, and on the x-axis it is time (ranging from September 13 to 17). Each tick mark on the x-axis is three hours.

The silicon planes of the two backward modules were damaged in the radiation incident. The bias currents drawn by these two modules are still a factor 2-3 higher than before the incident, figure 3.4. The quality of the data from the detector is still perfectly usable, with no significant changes in the distributions, so the VSAT is still working as

it should. The question remains, however, if it will survive yet another similar radiation incident, or if an automatic procedure should be set up in the VSAT slow controls system to force a LEP beam dump if the situation should arise again.

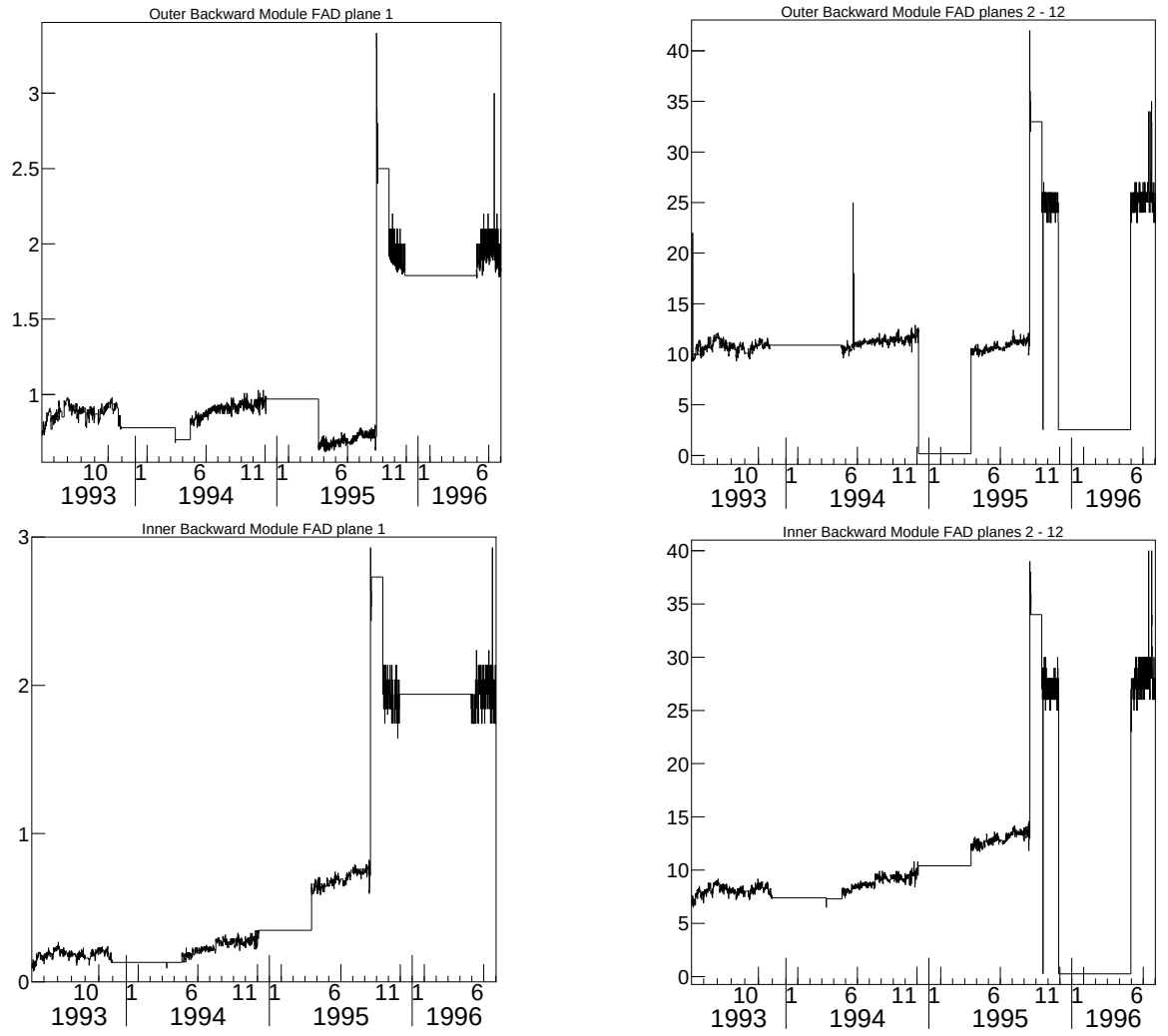

Figure 3.4: The bias currents drawn by the two backward VSAT modules, plane 1 and planes 2-12 shown separately, the outer modules on top and inner at the bottom. Unit on the y-axis is μA. The dips in the two plots to the right, at the the turn of the years 1994 and 1995, represents machine shutdowns when all electronics equipment was switched off.

3.3 STIC Slow Controls System

When the STIC detector replaced the Small Angle Tagger (SAT) in 1994, it was decided to use as much of the SAT slow controls system as possible for STIC. Three of the SAT sub-systems were altered to suit the STIC system:

BIAS: Used for supplying bias voltages to the silicon strip planes in the calorimeter.

FB: For monitoring and controlling the three STIC Fastbus crates.

TEMP: For monitoring the temperature at the front, sides and back of the calorimeters.

In addition to these, there were another four added to complete the STIC slow controls:

HV_C: Used for the calorimeter high voltage control. It contains two channels, one for each calorimeter module, and controls the main high voltage power supply. The output from this goes through a splitter system that distributes the high voltage to each read-out tetrode.

HV_E: Monitors the high voltages values and alarm, and the currents of each individual tetrode in the calorimeter high voltage system, *i.e.* the high voltages after the splitter system.

HV_V: This system controls the CAEN high voltage power supplies used for the Veto Counters.

POSI: For measuring the distance between the STIC modules and the surrounding sub-detectors.

This section includes only the parts of the system where I was personally involved in the development, except for the GSS and SMI sections in whose design I did not participate, but I still find it useful to explain them here because they differ slightly from the VSAT system.

3.3.1 BIAS and FB systems

Only a few changes were made to these systems. The BIAS system works exactly as described for the VSAT in 3.2.1. There are six channels, three per module. The changes mainly had to do with setting the correct voltage and which records in the status data base that should be updated.

The FB system was increased from two to three channels since STIC has three fastbus crates, while SAT only had two. The slow controls data base was altered accordingly. Also the monitoring of the Fastbus status was moved from the SAT SWST system to the FB system.

3.3.2 POSI system

The STIC modules have a larger radius than the previous SAT, and the gap between STIC and the surrounding end-cap detectors is much smaller. This makes it a critical situation for STIC whenever an end-cap is moved. To ensure that there is no damage done to the calorimeter when DELPHI is opened or closed, there are nine position sensors placed on each module: eight radial probes and one longitudinal.

The radial sensors are placed four in a ring around the calorimeter close to the front, and four in a ring close to the back. These measure the distance between the STIC and the Forward Ring Imaging CHerenkov counter (FRICH) supporting tube. The longitudinal probe is placed at the front of STIC measuring the distance to the TPC support. For each side there is also an additional channel that shows the voltage that is distributed to the probes.

All measurements made by the sensors are relative. There was no time to do an absolute calibration after they had been installed. Later on, a very rough calibration was made on one probe, which indicated that one ADC count on the output from the G64 corresponds to $\approx 2.5\mu$m. The system is designed such that the value increases with the distance. Thus, the monitored value should never approach zero.

Whenever an end-cap of DELPHI is moved, a close eye is kept on the read-out from the position probes to make sure that the STIC wont be damaged in the process.

The position information is also used during data-taking by the LEP control room. The STIC detectors are fixed at the end of the two superconducting quadrupoles. As a step in adjusting the beams, these quadrupoles are moved by the LEP control room which results in a clear correlation between the position of the STIC modules and the parameters of the beam. All position information is, since 1996, logged in the LEP Machine data base, which makes the information available on-line.

3.3.3 TEMP system

As mentioned in 1.2.8, the calorimeter is read out with high voltage driven phototetrodes, and it is necessary to monitor their temperatures. This is done by 32 temperature sensors, placed two in each sector in the vicinity of the tetrodes. A real overheating problem will show up on several sensors and gives the system a redundancy against malfunction.

There are also eight sensors placed on the side of each module, and eight at the front to report on the temperature in the environment of the STIC.

3.3.4 HV_V system

The veto counters in front of the calorimeter are connected to a CAEN high voltage power supply. The values of the output from these is not accessible in the slow controls system. However, the status of the CAEN crate is monitored, and it is possible to switch it on or off as well. This monitoring/control of the CAEN was put in the HV_V system.

3.3.5 GSS Systems

As for the VSAT slow controls system, STIC also has two GSS objects. Their alarm states generate similar actions as for the VSAT, *i.e.* an alarm from the detector object cuts all high and low voltages, while an alarm from the counting room object cuts power to the electronics crates.

After an alarm from the counting room object has been cleared, it is necessary to visually check that the high voltage systems come back normally before the AL_CANCEL state can be cleared. The power supply for the calorimeter (HV_C system) may need to be reset before the high voltages can be raised.

The CAEN power supply for the veto counters (HV_V system) should also be checked. This is done by a program on a nearby terminal which shows the status of individual channels. If all are off, then the CAEN crate needs to be reset, while if only some channels are off, these are switched on by use of the program itself.

3.3.6 SMI States, Actions and Recoveries

There are seven elementary obects for STIC. In addition to these there are of course the CL and SC objects, but also one object called *LEP_RELATED* and one called *RUN_RELATED*. These are necessary because the STIC is sensitive to different LEP activities, *e.g.* when LEP is being filled the high voltages should be at an intermediate setting, called *STANDBY* values, to reduce the risk of damage should the background be high.

The HV_C and HV_V have a few additional states and commands, not listed in tables 3.1 and 3.2, that are required for high voltage systems. Some ot these states could be used also for the low voltage bias system, namely the *CHANGING*, *HELD_OFF*, and *RUN* states. However, I did not find it useful to add them to the BIAS object since the bias voltages are always ON, and should they be ramped up or down, it is such a fast action that the CHANGING state is unnecessary. These states are more useful for high voltage channels that takes minutes to ramp, and where the possibility of inhibiting commands can be useful so that the voltages are not raised or lowered by misstake. The additional states are listed in tables 3.5 and 3.6.

Table 3.5: Additional SMI states of the high voltage elementary objects defined in the STIC SMI logics.

SMI state	Condition
CHANGING	At least one channel is ramping up or down and at least one channel is above STANDBY level.
CHANGING_LO	At least one channel is ramping up or down and all channels are at or below STANDBY level.
ERROR_LO	At least one channel is out of range and all channels are at or below STANDBY level.
HELD_OFF	Same as OFF, but an explicit RELEASE command is required before any control is possible.
RUN	Same as ON, but an explicit RELEASE command is required before any control is possible.
STANDBY	All channels are at their intermediate level.

Table 3.6: Additional SMI commands of the high voltage elementary objects defined in the STIC SMI logics.

SMI Command	Action
HOLD	If the state is ON or OFF, inhibits further commands.
RELEASE	Cancels the HOLD command.
REPAIR	Ramps channels that have tripped to their present settings.
STANDBY	Ramps channels to their intermediate values.

The STIC CL object is identical to that of VSAT. The SC object has an additional state *CHANGING* which indicates that one of its high voltage system is currently ramping at least one channel up or down. There are a few additional central SMI commands processed because of the presence of high voltages. These are shown in table 3.7. The

actions taken for these commands depend on how sensitive the sub-detector is to LEP beam activities. The STIC is fairly unsensitive, so the high voltages can be ramped up already when LEP is in *coarse tuning* mode, *i.e.* when the machine has been filled and the beams are tuned.

Table 3.7: Additional central SMI commands of the STIC SC object defined in the SMI logics.

SMI Command	Action
C_PREPARE_FOR_COARSE_TUNING	Ramps high voltages to ON.
C_PREPARE_FOR_DUMP	Ramps high voltages to STANDBY.
C_PREPARE_FOR_INJECTION	Ramps high voltages to STANDBY.
C_PREPARE_FOR_SHUTDOWN	Ramps high voltages to STANDBY.
C_RESPOND_TO_BACKGROUND	Nothing.

The RUN_RELATED object has only two states: READY when all subsystems are ready for data-taking, and NOT_READY when at least one of HV_C, HV_V or FB is in error or changing states. This object is used by the automatic control system of DELPHI, where a number of important detectors are defined. If any of these go into NOT_READY state, data-taking automatically stops until the problem is cleared and all are back in READY.

The LEP_RELATED object indicates the level of LEP beam operation permissible taking into account the high voltage status of the sub-detector. It also receives commands from the central operator to adjust high voltages to the appropriate level considering desired LEP beam activity. For the STIC there are two possible states for the LEP_RELATED object: ALLOW_BEAM_CT which allows coarse tuning, but not dump or injection, and ALLOW_BEAM_CT_D_INJ which allows any LEP activity. The commands accepted are the first three in table 3.7. Whenever LEP prepares for an activity that isn't allowed by all sub-detectors with a LEP_RELATED object, *e.g.* prepares for injection while STIC shows ALLOW_BEAM_CT, it is the responsibility of the DELPHI shift leader to inform the LEP control room that there is a problem in DELPHI that needs to be solved before the activity in question can be started.

The VSAT error recovery procedures presented in 3.2.5 are the same for the STIC objects, however, the ERROR list entry should be extended to include the objects that don't exist in the VSAT system:

ERROR: The procedures for the additional objects are: HV_C — give a command that ramps up all high voltage channels; HV_E — this process is only monitoring and cannot control anything, therefore an error in HV_E should lead to a ramp-up command for object HV_C; HV_V — ramp up the tripped channels using a special program that runs on a dedicated terminal in the counting room; POSI — the low voltage for the sensors is off, contact the STIC expert; TEMP — the temperature is out of the desired range, contact the STIC expert.

Chapter 4

Two-Photon Physics

Photon-photon interaction in vacuum is not allowed in the classical electromagnetic theory. In order to describe such interactions one has to use the *Quantum ElectroDynamic theory* (QED). However, the probability for these interactions is extremely small at low energies, which prevents them from being observed with even the strongest of photon beams, *e.g.* lasers.

By QED radiative quantum effects, electrons and positrons in motion are surrounded by clouds of virtual photons. Thus, the circulating e^+e^- beams of an electron-positron collider, *e.g.* PETRA, PEP, LEP, *etc.*, can be used as the sources of strong photon beams, and provide an excellent opportunity to study photon-photon reactions in collisions of the photon clouds surrounding the beam particles. High energy electrons can split off low-$p_\perp$ photons with a life time of order $t \sim \frac{E}{p_\perp^2}$ where E is the beam energy and $p_\perp$ is the γ transverse momentum relative to the beam direction. Time dilatation renders this lifetime much longer than typical reaction times of order 10^{-23} s so that the low-$p_\perp$ photons can well be treated as real particles in a scattering process.

The photons are radiated according to a bremsstrahlung spectrum with probability $\sim 1/E_\gamma$, and mainly into small angles ($\sim m_e/E$) relative to the beams. This implies a dominance of two-photon events with low invariant mass W. The visible photon luminosities are only about one order of magnitude smaller than the e^+e^- luminosities.

In e^+e^- collisions the kinematics is fixed by the beam energy to lowest order. Not so in the photon-photon reactions where the energy spectra of the photons allow different values of W to be measured. Normally the two interacting photons have different energies, and therefore most two-photon center of mass frames are boosted along the e^+e^- beam direction. Since particle production is concentrated at low $p_\perp$ (unlike annihilation processes like $e^+e^- \to \gamma^*/Z^0 \to q\overline{q}$), some produced particles will go undetected inside the beam pipe or in cracks between different forward trackers and calorimeters, making the visible (detected) cross section smaller than the true (produced) cross section.

With the high energies available at PETRA and PEP two-photon processes became measurable in a large kinematical range. Since then two-photon studies have become more important and have been performed by a number of e^+e^- experiments, *e.g.* by PLUTO [24] at DESY, by TPC/2γ [25] at SLAC, and by AMY [26] at KEK. All four LEP experiments have also presented results on two-photon physics (ALEPH [27], DELPHI, L3 [28], and OPAL [29]).

This chapter contains a short introductory theoretical background to the field of two-photon physics, followed by some two-photon results obtained with the DELPHI detector, with emphasis on the analysis of VSAT double-tagged events.

Presently LEP is running in the so called LEP2 phase with beam energies $E_{beam} \approx$ 81 GeV, where the ratio between the cross section of two-photon events and events of other processes, *e.g.* Z^0-production, is much higher, and the dominant inelastic process at LEP2 is the two-photon process. However, my analysis has been done on data taken from 1991 to 1993, in the LEP1 phase, with beam energy of $E_{beam} \approx 45.6$ GeV, and whenever I refer to E_{beam} in the text, it is assumed to be LEP1 energy.

4.1 Theoretical Background

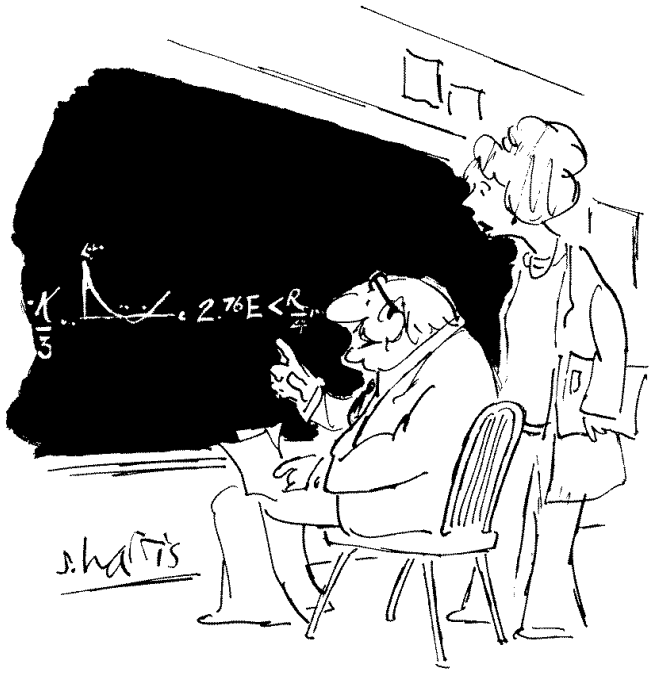

"THE BEAUTY OF THIS IS THAT IT IS ONLY OF THEORETICAL IMPORTANCE, AND THERE IS NO WAY IT CAN BE OF ANY PRACTICAL USE WHATSOEVER."

This section gives a brief introduction to the theory of two-photon physics. It starts with a discussion on the competing processes before turning to two-photon kinematics, models, cross section, structure functions, and experimental techniques.

4.1.1 Processes

The reaction $e^+e^- \rightarrow e^+e^-X$, where X is a particle system can be classified by four different processes:

- Virtual Bremsstrahlung processes with e^+e^- scattering. In this process we have elastic scattering of the incoming beam leptons. The bremsstrahlung is an initial or final state radiation where the emitted photon splits into a $q\overline{q}$ pair which cascades into a particle system, figure 4.1a.

- Virtual Bremsstrahlung processes with e^+e^- annihilation. This process is similar to the previous one with the exception that the incoming e^+e^- annihilate into a γ (or Z^0) and then produce a new e^+e^- pair, figure 4.1b.

- γ cascade processes, where the incoming e^+e^- annihilate into a γ^* or Z^0, which decays into a $q\overline{q}$ pair, where the quark or anti-quark emits a photon that splits into an e^+e^- pair. This process is then similar to the one in figure 4.1b with the e^+e^- and $q\overline{q}$ pairs exchanged. The process is described in figure 4.1c.

- Two-photon processes, where two photons, one from each incoming beam lepton, collide to produce a particle system, figure 4.2.

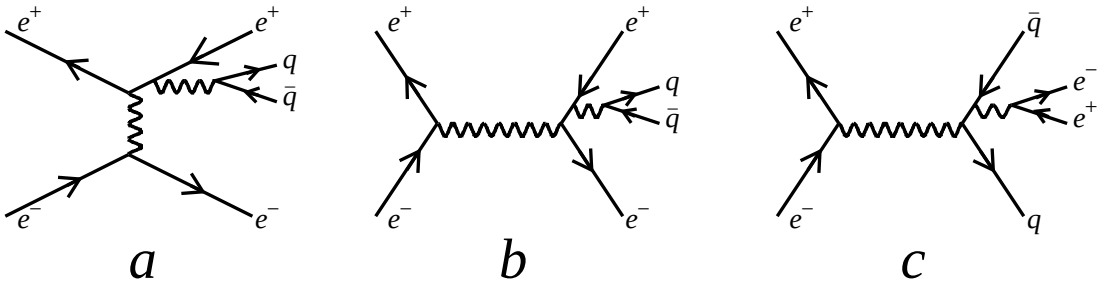

Figure 4.1: Feynman diagrams of **a**) the virtual bremsstrahlung process with e^+e^- scattering, **b**) the virtual bremsstrahlung process with e^+e^- annihilation, and **c**) the γ cascade process.

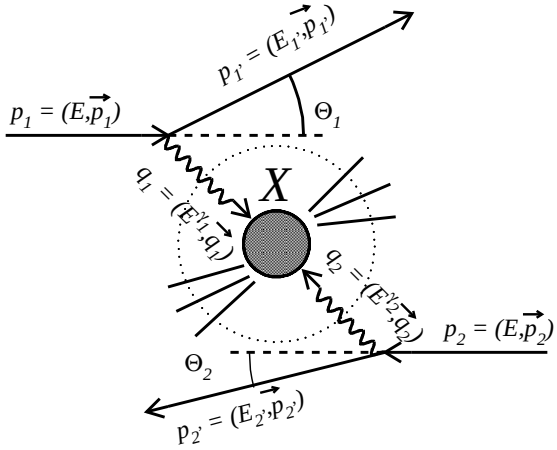

Figure 4.2: The two-photon process with description of the kinematics of the reaction.

In each of these processes, the photon propagator can be exchanged to a Z^0 boson. In the processes 4.1a and 4.2 the diagrams with the Z^0 boson propagator will be strongly

suppressed due to the very high mass of the Z^0 boson ($m_{Z^0} = 91.187 \pm 0.007$ GeV/c^2, PDG 1996), and will not be considered for the purpose of this thesis.

In the processes in figure 4.1b and c, the final state e^+e^- are emitted in any angles, and requiring detection of these particles in small angular ranges, or not detecting them at all, suppresses the contribution of these diagrams to the total cross section. In the process shown in figure 4.1a one of the scattered beam leptons will have an energy close to the beam energy, and the contribution from this diagram can be suppressed by tagging the scattered leptons and requiring that both the scattered beam particles should have lost at least some 10% of their initial energy.

4.1.2 Kinematics

In the two-photon process, the momentum transfer of an $e\gamma \rightarrow e\gamma$ vertex is calculated from the four-momentum of the radiated photon.

$$-Q_i^2 = q_i^2 = (p_i - p_i')^2 = 2m_e^2 - 2E_i E_i'(1 - \sqrt{1 - \frac{m_e^2}{E_i}}\sqrt{1 - \frac{m_e^2}{E_i'}}\cos\theta_i). \tag{4.1}$$

The incoming lepton energy E_i is equal to the beam energy. In the case of LEP, we can notice that $m_e/E \sim 10^{-5}$, and since we are tagging the scattered leptons at angles $\theta \gg m_e/E$ and with $E_{tag}/E_{beam} > 0.4$ we can approximate equation (4.1) by

$$-Q_i^2 = q_i^2 \approx -4E_{beam}E_i' \sin^2\frac{\theta}{2} \tag{4.2}$$

The invariant mass of the produced particle system X is calculated from the four-momenta of the interacting photons

$$W^2 = (q_1 + q_2)^2. \tag{4.3}$$

With q_i, as mentioned before, given by $q_i = p_i - p_i'$, and the photon energy $E_i^\gamma = E_{beam} - E_i'$, this will be

$$W^2 = 4E_1^\gamma E_2^\gamma - 2E_1'E_2'(1 - \cos\theta_1\cos\theta_2 - \sin\theta_1\sin\theta_2\cos\Phi), \tag{4.4}$$

where Φ is the angle between the two planes defined by the two $e\gamma \rightarrow e\gamma$ systems. When analysing events with a very small θ angle, of the order of mrad, one can simplify equation (4.4) to

$$W^2 \approx 4E_1^\gamma E_2^\gamma. \tag{4.5}$$

4.1.3 Models

The photon shows several different characteristics and is therefore a complex object to describe. In some experiments, *e.g.* high energy e^+e^- annihilation, it shows a direct coupling to pointlike quarks. In other experiments, *e.g.* photoproduction, electromagnetic form factors *etc.*, it shows characteristics of soft hadron interactions. For the description of $\gamma\gamma$ physics, the case of coupling to pointlike quarks is described by the QPM model,

and the soft hadron interactions by the VDM model. However, a combination of these two models is not enough to describe data from recent experiments [35–37]. Therefore, a third component, the QCD-based hard scattering model, has been added. This model requires a specific Parton Density Function (PDF) to calculate parton momentum fractions, and there is a large number of parametrizations of the photon to choose from.

The total cross section for $\gamma\gamma$ interactions can be described as

$$\sigma_{tot} = \sigma_{low-p_\perp} + \sigma_{jet} \tag{4.6}$$

The $\sigma_{low-p_\perp}$ part is represented by the non-perturbative VDM model. The σ_{jet} part consists of direct, single-resolved, and double-resolved contributions, where the direct part is described by the QPM model, and the single- and double-resolved parts correspond to the QCD-RPC model. Thus, we can alternatively write σ_{tot} as

$$\sigma_{tot} = \sigma_{VDM} + \sigma_{QPM} + \sigma_{QCD-RPC} \tag{4.7}$$

This subdivision is a convenient starting point, but should only be seen as a first approximation. An interplay between theory and experiments can help clarify the picture.

In the models, the two photons are assumed to be quasi-real, and this is indeed the case since their average squared masses, as obtained from Monte Carlo studies, are of the order 0.1 GeV^2/c^4.

Below is a brief introduction to each model, and in section 4.1.4 the cross sections of the σ_{jet} part will be discussed.

VDM Model

The Vector meson Dominance Model (VDM) is a non-perturbative, phenomenological model. It was developed about 20 years ago, as an attempt in relating $\gamma - \gamma$ and γ-hadron collisions to hadron-hadron interaction physics. VDM is designed to describe the low-$p_\perp$ part of these collisions.

To describe the interaction between a photon and a hadron, VDM assumes that the photon part of the time exists as virtual fluctuations to $q\overline{q}$ pairs. For small transverse momenta in the virtual branching $\gamma \to q\overline{q}$, $p_\perp < \mathcal{O}(\Lambda)$, where Λ is the QCD-scale of a few hundred MeV, the lifetime of the formed quark-antiquark pair is long and the overlap with the low-lying resonances ρ, ω, and ϕ is large. This defines the VDM component of the photon. The vector mesons states then interact with hadrons through the strong force, figure 4.3. The main contribution to the total $\gamma\gamma$ cross section comes from VDM processes. Photon-photon interaction will, thus, have the characteristics of hadron-hadron interactions.

A parametrization of VDM $\gamma\gamma$ cross section, as used in the two-photon analysis at DELPHI, is given by [38]

$$\sigma_{\gamma\gamma}(W^2, Q^2, P^2) = F_{VDM}(Q^2) F_{VDM}(P^2) \left[A + \frac{B}{W} \right], \tag{4.8}$$

where W is the invariant mass of the two-photon system and Q^2 and P^2 are the squared masses of the two virtual photon. Comparison with measured cross sections yields $A =$

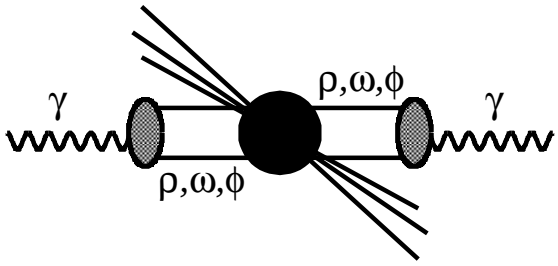

Figure 4.3: Diagram of the VDM contribution to the two-photon multi-hadronic state X.

275 nb and $B = 300$ nb $\cdot$ GeV [39]. This type of parametrization has already been used by previous experiments [24,26]. The quantity F_{VDM} is the generalized VDM form factor [40], and can be parametrized from experimental data to be

$$F_{VDM}(Q^2) = \sum_{V=\rho,\omega,\phi} r_V \frac{1 + Q^2/4m_V^2}{(1 + Q^2/m_V^2)^2} + \frac{0.22}{1 + Q^2/m_0^2}, \tag{4.9}$$

where m_V denotes the vector meson mass and r_V is related to coupling of vector meson V to the photon. The r_V values used were $r_\rho = 0.65$, $r_\omega = 0.08$, and $r_\phi = 0.05$. The last term, where the value $m_0 = 1.4$ GeV was used, describes the contribution from the radial excitations of the vector mesons.

QPM Model

Photons can exhibit pointlike couplings directly to a quark-antiquark pair, which subsequently fragments into hadrons. The resulting events show typical two-jet topologies. This process is described by the Quark Parton Model (QPM), figure 4.4, and it is also called the direct process.

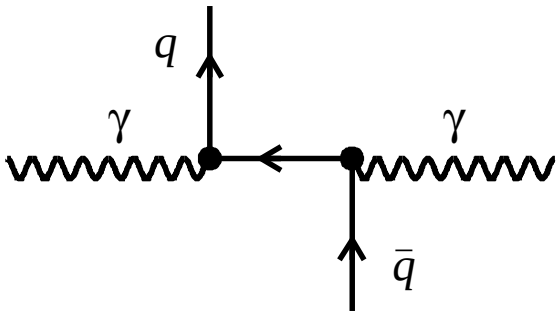

Figure 4.4: Lowest order diagram of the QPM contribution to the two-photon multi-hadronic state X.

If the transverse momentum of the quark in the photon splitting process is large, $p_\perp > \mathcal{O}(\Lambda)$, the lifetime of the formed $q\overline{q}$ state becomes so short that the pair cannot couple to a vector meson anymore, and the quark acts as a perturbative propagator between the two photons.

Contrary to VDM, QPM is only applicable at large Q^2, high quark $p_\perp$, or high quark masses. The lifetime of these states are too short for the formation of bound states.

The contribution to the total cross section from QPM is in general comparatively small at the relatively low Q^2 of most two-photon events, while at large Q^2 it becomes proportionally more important since it falls off slower than the other processes contributing to the cross section.

QCD-RPC Model

Since a photon can fluctuate into a $q\overline{q}$ pair, which can fluctuate further to more complicated partonic states, it is possible to define Parton Density Functions (PDF's) for the photon, as for a hadron. These PDF's are used in the QCD Resolved Photon Contribution (QCD-RPC) model, which is a third component needed to describe two-photon data at low Q^2. In this, one photon in the single resolved, and both photons in the double-resolved processes, fluctuate into partonics states, figure 4.5.

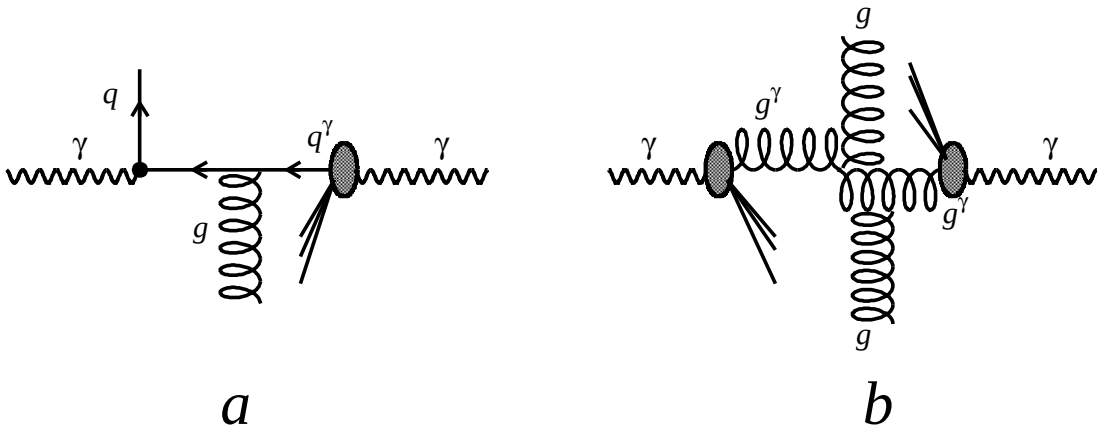

Figure 4.5: Lowest order diagrams of the QCD-RPC contribution to the two-photon multihadronic state X. **a)** shows the single-resolved, and **b)** the double-resolved contributions.

The scattered partons will produce high-$p_\perp$ jets, while the spectator partons produce remnant jets. In the single-resolved case we have a remnant jet on one side, and in the double-resolved case there is a remnant jet on each side of the event vertex. These remnants are mainly produced at very small angles, making them difficult to detect in full, and gives the QCD-RPC event shapes similar to the high-$p_\perp$ two-jet topologies of the QPM events.

To calculate the cross section from the QCD-RPC model, it is necessary to use Parton Density Functions (PDF). The PDF's give, for each parton, the parton density for a given (x,Q^2) value, where x is the fraction of the total hadron longitudinal momentum carried by a given parton.

There are many different parametrizations of the photon parton density available, but some of them cannot be used for hard scattering at relatively low $p_\perp^2/c^2$ since they are derived from deep inelastic $e\gamma$ scattering at high Q^2. There are a few PDF's which all agree fairly well with data, and their main differences are from their behaviour at low x, and how they parametrize gluons at large x. With the current data available, it is not clearly possible to favour any of them, but with LEP2 data, which will reach to lower x values and also give higher statistics, the situation may improve.

4.1.4 Cross Section

Calculation of the two-photon cross section is a very complicated matter. For the purpose of this thesis we are mainly interested in $\sigma(\gamma\gamma \rightarrow \text{hadrons})$ part. When doing the calculations one can start in either of two extreme cases. One is where the cross section $\sigma_{jet}^{\gamma\gamma}$ is calculated from the contributions of the possible feynman diagrams, and describes the high-$p_\perp$ contribution to the cross section. The other is needed to also describe the low-$p_\perp$ contribution to the $\gamma\gamma$ cross section, where one start with parametrizations of pp and $p\overline{p}$ cross sections and derive expressions for γp and $\gamma\gamma$ processes.

We start here with the feynman diagram approach. The three sub-processes are shown in figure 4.6, where a) is direct, b) is single-resolved, and c) is the double-resolved contributions. In b and c one or both photons have fluctuated into a $q\overline{q}$ state and a parton from each of these interact, while the rest continues as the remnant.

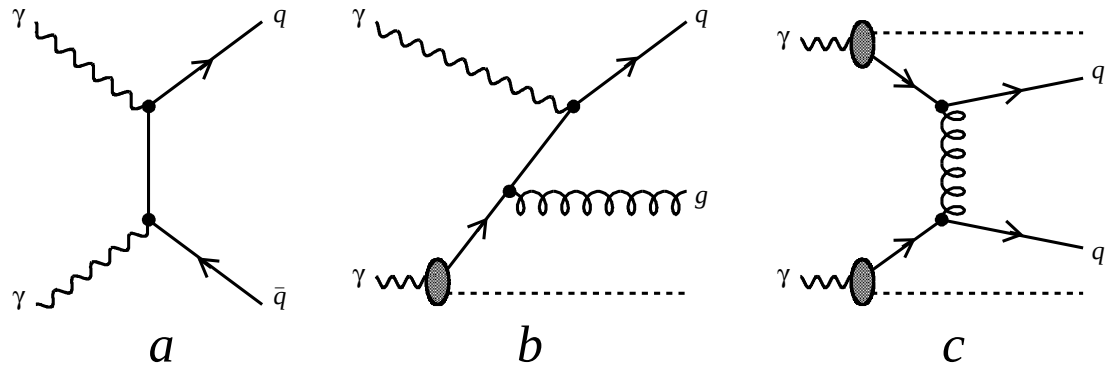

Figure 4.6: Examples of Feynman diagrams of the process $\gamma\gamma \rightarrow q\overline{q}$. **a**) shows the direct contribution, **b**) the single-resolved contribution, and **c**) the double-resolved contribution.

At a first glance on these diagrams, one sees that the first one is suppressed by a factor α_{em}^2, while the second only seem to have α_{em} and the third is without α_{em}. This is not true, since in the single- and double-resolved case one or two photons convert to a partonic state, and this process is governed by the Photon Structure Function in which α_{em} appears. Thus, all three diagrams contain the factor α_{em}^2.

The cross section $\sigma_{jet}^{\gamma\gamma}$ is then the sum of the contributions from these diagrams

$$\sigma_{jet}^{\gamma\gamma} = \sigma_{direct}^{\gamma\gamma} + \sigma_{1-res}^{\gamma\gamma} + \sigma_{2-res}^{\gamma\gamma} \tag{4.10}$$

where, as discussed in 4.1.3, the direct process is described by the QPM model, and the single- and double-resolved processes correspond to the perturbative QCD-RPC model. These three terms can be calculated separately. When looking at two-photon events with a very small momentum transfer, we have $Q^2 \ll |\hat{t}|$ and we can neglect all terms with a $Q^2/\hat{t}$-dependence in the calculations below. (They would be available in a complete description.)

The cross section for the direct contribution can be found to be [32]

$$\frac{d\hat{\sigma}}{d\hat{t}}(\gamma\gamma \rightarrow q\overline{q}) = e_q^4 \frac{2\pi\alpha^2}{\hat{s}^2} \frac{\hat{t}^2 + \hat{u}^2}{\hat{t}\hat{u}}. \tag{4.11}$$

This is symmetric in the $\hat{t}$ and $\hat{u}$ channels since interchanging $\hat{t} \leftrightarrow \hat{u}$ correspond to interchanging $q \leftrightarrow \overline{q}$. The expression diverges for $\hat{t} \to 0$ and $\hat{u} \to 0$. If we make the approximation $-\hat{t} \ll \hat{s}$, then $p_\perp^2 \approx -\hat{t}$ and $\hat{u} \approx -\hat{s}$ and we get the following expression for the cross section

$$\frac{d\hat{\sigma}^{\gamma\gamma}_{direct}}{dp_\perp^2} \approx e_q^4 \frac{2\pi\alpha^2}{\hat{s}} \frac{1}{p_\perp^2}. \tag{4.12}$$

The $\hat{u} \to 0$ gives an equally large additional contribution. We can clearly see that the cross section is divergent for $p_\perp^2 \to 0$.

The single-resolved case can be represented by the $\gamma q \to qg$ scattering process. The cross section for this process is given by

$$\frac{d\hat{\sigma}}{d\hat{t}} = \frac{8\pi e_i^2 \alpha \alpha_s}{3\hat{s}^2} \left(-\frac{\hat{t}}{\hat{s}} - \frac{\hat{s}}{\hat{t}} \right) \tag{4.13}$$

If we again make the approximation $-\hat{t} \ll \hat{s}$, then $p_\perp^2 \approx -\hat{t}$ and we get

$$\frac{d\hat{\sigma}^{\gamma\gamma}_{1-res}}{dp_\perp^2} \approx \frac{8\pi e_i^2 \alpha \alpha_s}{3\hat{s}} \frac{1}{p_\perp^2} \tag{4.14}$$

As for the case of the direct contribution, this cross section is divergent for $p_\perp^2 \to 0$. Also the other single-resolved process, $\gamma g \to q\overline{q}$, has a $p_\perp^{-2}$ behaviour.

In the case of the double-resolved contribution there are several subprocesses, $q_i q_j' \to q_i q_j'$, $qg \to qg$, $gg \to gg$, $q_i \overline{q}_i \to q_j \overline{q}_j, i \neq j$ and $i = j$, $q_i \overline{q}_i \to gg$, and $gg \to q_i \overline{q}_i$. The last three subprocesses correspond to either gluon exchange in the s-channel or quark exchange in the t-channel, whereas the first three are dominated by gluon exchange in the t-channel.

The process in figure 4.6c is $q_i q_j' \to q_i q_j'$, and its cross section is given by

$$\frac{d\hat{\sigma}}{d\hat{t}}(q_i q_j' \to q_i q_j') = \frac{4}{9} \frac{\pi \alpha_s^2}{\hat{s}^2} \frac{\hat{s}^2 + \hat{u}^2}{\hat{t}^2} \tag{4.15}$$

As previously we can approximate $p_\perp^2 \approx -\hat{t}$ and we see that the cross section is proportional to $p_\perp^{-4}$:

$$\frac{d\hat{\sigma}}{dp_\perp^2}(q_i q_j' \to q_i q_j') \approx \frac{8\pi\alpha_s^2}{9} \frac{1}{p_\perp^4} \tag{4.16}$$

As seen for the direct and single-resolved processes, quark exchange in the t-channel corresponds to a $p_\perp^{-2}$ singularity in the cross section, while the gluon exchange in the t-channel gives a $p_\perp^{-4}$ singularity, equation (4.16). The first three subprocesses of the double-resolved case are therefore more important at low-$p_\perp$ events. These differ from each other by the number of interacting gluon and quarks. For each quark that is replaced by a gluon, the cross section of the process is roughly multiplied by a factor 9/4 due to color charge.

Having extracted the $p_\perp$ dependence of the different possibilities of jet-production processes in figure 4.6 we can now argue in which $p_\perp$-regions they are significant. In the

direct case we have a $p_\perp^{-2}$ dependence. We can also note all the energy of both photons is available for the reaction. In the single-resolved case we have the same $p_\perp$ dependence, but here one photon has split into a partonic state, and the parton that interact with the other photon will most probably have lower energy than the initial photon. This suppresses the process in the high-$p_\perp$ region, while leading to an enhancement for low-$p_\perp$ events compared to the direct process. For the double-resolved contribution both photons have split into partonic states; this gives a stronger suppression for high-$p_\perp$ events than for the single-resolved case. For low-$p_\perp$ events the $p_\perp$ dependence goes like $p_\perp^{-4}$ and this renders the double-resolved process the most significant in this region.

All cross sections above diverge for $p_\perp \to 0$. This is regulated by a number of non-perturbative phenomena, including effective quark masses and hadronic wave functions, that we do not (yet) understand. For using these equations to describe the $\gamma\gamma$ cross section, one needs to introduce some perturbative cut-off $p_\perp^{min}$, below which the calculations are invalid.

In order to describe the total $\gamma\gamma$ cross section one must therefore pick another starting point. It is possible to start with the familiar hadronic cross sections [33]

$$\sigma_{tot}^{AB}(s) = X^{AB} s^{\epsilon} + Y^{AB} s^{-\eta} \tag{4.17}$$

for $A + B \to X$. The powers ϵ and η are universal, with fit values [34]

$$\epsilon \approx 0.0808, \qquad \eta \approx 0.4525, \tag{4.18}$$

while the coefficients X^{AB} and Y^{AB} are process-dependent. Equation (4.17) can be interpreted within Regge theory, where the first term corresponds to Pomeron exchange and gives the asymptotic rise of the cross section, and the second term is the reggeon one.

In pp and $p\overline{p}$ collisions this parametrization of the cross section has shown good agreement with the data. Recently it has been shown at the HERA collider at DESY that a similar parametrization can be used for γp data:

$$\sigma_{tot}^{\gamma p}(s) \approx 67.7 s^{\epsilon} + 129 s^{-\eta} [\mu b], \tag{4.19}$$

with s in GeV^2. We can then take the Regge-theory ansatz seriously for the photon and derive an expression for the total $\gamma\gamma$ cross section

$$\sigma_{tot}^{\gamma\gamma}(s) \approx 211 s^{\epsilon} + 215 s^{-\eta} [nb]. \tag{4.20}$$

Note that the units of the cross section in these parametrizations is mb for pp and $p\overline{p}$ collisions, μb for γp, and nb for $\gamma\gamma$.

Here we have made the assumptions that the pomeron and reggeon terms factorize, $X^{AB} = \beta_{AIP}\beta_{BIP}$ and $Y^{AB} = \gamma_{AIP}\gamma_{BIP}$, so that $X^{\gamma\gamma} = (X^{\gamma p})^2/X^{pp}$ and $Y^{\gamma\gamma} = 2(Y^{\gamma p})^2/(Y^{pp} + Y^{p\overline{p}})$, with $X^{pp} \approx 21.7$ [mb] and $(Y^{pp} + Y^{p\overline{p}})/2 \approx 77.23$ [mb]. In hadronic cross sections, factorization seems valid for the pomeron term but not for the reggeon one. The choice of using the average of Y^{pp} and $Y^{p\overline{p}}$ is an arbitrary one, though it can be motivated by arguments of counting the number of allowed valence quark/antiquark annihilation/exchange diagrams possible in the various processes. The $Y^{\gamma\gamma}$-term only affects the low-energy behaviour and the choice of Y^{pp}, $Y^{p\overline{p}}$, or their average is not critical for us. Comparisons with data show that this Regge-theory approach is so far valid. However, a real test will be to include LEP1 and LEP2 data in the comparison.

4.1.5 The Photon Structure Function

In a single-tagged two-photon events the target photon can be assumed to be almost on-shell, and the whole process can be viewed as deep inelastic scattering of the tagged lepton off the quasi-real target photon with a squared mass P^2 around zero. This deep inelastic electron-photon scattering offers a complementary method to investigate QCD in e^+e^- collisions. As discussed before the photon can fluctuate into partonic states such as a hadron, and just as one can define parton contents of hadrons, this is done for photons by introducing the photon structure function. The Altarelli-Parisi equations describe the Q^2 evolution of PDF's by splittings of partons, *i.e.* $q \to qg$, $g \to q\overline{q}$, and $g \to gg$. For the photon there is an additional term corresponding to $\gamma \to q\overline{q}$ which renders the equations inhomogeneous, and gives rise to the structure function increasing linearly with $\ln Q^2$ in leading order.

Definitions of the Photon Structure Functions

The cross section for deep inelastic electron scattering off a photon target is parametrized by two structure functions:

$$\frac{d\sigma}{dxdy} = \frac{16\pi\alpha^2 E E_\gamma}{Q^4}[(1-y)F_2^\gamma(x,Q^2) + y^2 x F_1^\gamma(x,Q^2)] \tag{4.21}$$

F_1^γ and F_2^γ are proportional to the cross sections for transversely and longitudinally polarized virtual photons

$$\begin{aligned} F_1^\gamma &= F_T^\gamma \\ F_2^\gamma &= 2xF_T^\gamma + F_L^\gamma \end{aligned} \tag{4.22}$$

The momentum transfer $q^2 = -Q^2$ and the energy transfer $\nu = qp_\gamma$ can be expressed in terms of the energy of the target photon E_γ, the electron energies E and E' before and after the collision, and the scattering angle θ in the laboratory system:

$$\begin{aligned} Q^2 &= 4EE'\sin^2\frac{\theta}{2} \\ \nu &= 2E_\gamma(E - E'\cos^2\frac{\theta}{2}) \end{aligned} \tag{4.23}$$

The invariant final-state hadron mass W is given by ν and Q^2

$$W^2 = 2\nu - Q^2 \tag{4.24}$$

and the Bjorken variable x and y are related to these observables by

$$\begin{aligned} x &= \frac{Q^2}{2\nu} = \frac{Q^2}{Q^2 + W^2} \\ y &= \frac{\nu}{kp_\gamma} = 1 - \frac{E}{E'}\cos^2\frac{\theta}{2} \end{aligned} \tag{4.25}$$

The coefficient y^2x in equation (4.21) is very small under normal experimental conditions so that only $F_2^\gamma(x,Q^2)$ can be measured.

In the simple parton model, F_2^γ is given by

$$F_2^\gamma(x,Q^2) = \sum_q e_q^2(xq^\gamma(x,Q^2) + x\overline{q}^\gamma(x,Q^2)) \tag{4.26}$$

Note that $q^\gamma(x,Q^2) \sim e_q^2$ (and similarly $\overline{q}^\gamma(x,Q^2) \sim e_q^2$) and hence the total charge contribution to F_2^γ is $\sim e_q^4$.

Predictions of the Structure Functions

The theory of the photon structure function had been gradually developed over a decade before deep-inelastic electron-photon scattering became experimentally accessible at the high-energy e^+e^- colliders. The important qualitative features of the experimental results conform with the theoretical predictions — a non-trivial test of QCD.

Space-time analysis of electron-positron scattering reveals the complex nature of this reaction. Depending on the transverse momentum of the quark in the photon splitting process, two different components can be distinguished.

As mentioned in section 4.1.3 the photon can form bound states of vector mesons. Adopting counting rule arguments and attributing half of the vector-meson momentum to quarks, the quark density is taken to be $\approx \frac{1}{2}(1-x)/x$. This parametrization is backed up by measurements of quark and gluon densities in pions. This VDM component decreases with increasing Q^2 for $x \geq 0.2$ similarly to the nucleon structure function.

When the lifetime of the formed quark-antiquark pair is too short to form a bound vector meson state, see section 4.1.3, the QPM model is used for describing the two-photon reaction. Neglecting gluon bremsstrahlung, this component is given, in the parton approach, by

$$F_2^{\gamma,PART} = \frac{3\alpha\sum e^4}{\pi} x[x^2+(1-x)^2]\ln\frac{Q^2}{Q_0^2} \tag{4.27}$$

$$F_L^{\gamma,PART} = \frac{12\alpha\sum e^4}{\pi} x^2(1-x)$$

where the sum $\sum e^4$ runs over all quark flavors, and Q_0 a lower limit for when $F_2^{\gamma,PART}$ is valid for describing the photon structure. Below this Q_0 limit, the $F_2^{\gamma,VDM}$ function is needed. The leading part of F_2^γ is linear in $\ln Q^2$, while F_L^γ is asymptotically finite and scale invariant.

The contribution of heavy quarks to the photon structure function is well described by the quark parton model. The production process extends only over a distance of the order of the Compton wave length of the heavy quark and gluon bremsstrahlung is suppressed, so that the zeroth order QCD calculation is adequate. The Coulombic gluon rescattering corrections rendering F_2^c non-zero at threshold are restricted to a small domain near $x \leq Q^2/(Q^2+4m^2)$. The production of b quarks is doubly suppressed by the higher mass as well as the reduced electric charge $e_b^4/e_c^4 = 1/16$.

After switching on perturbative gluon radiation, three mechanisms compete with each other to build up the structure function F_2^γ in the leading order. With rising Q^2,

- the number of quarks rises at a fixed x due to the increasing $\gamma \to q\overline{q}$ splitting probability;

- at $x \geq 0.4$ quarks are lost due to increasing gluon radiation (the quarks accumulate at small x);
- gluon radiation is damped as a consequence of the logarithmically decreasing coupling constant.

The net effect, after solving the Altarelli-Parisi equations asymptotically for quark and gluon densities is a structure function that keeps rising linearly in $\ln Q^2/\Lambda^2$ (at not too small x) but with an $\mathcal{O}(1)$ change of the coefficient.

4.1.6 Experimental Techniques

By having electromagnetic calorimeters in the forward and very forward regions of the experimental detector setup, it is possible to detect one or both of the scattered beam particles. However, the leptons may still be undetected due to never leaving the beam pipe, or traveling in gaps that normally exists between the forward and very forward detectors. Detection of the scattered leptons is called *tagging*. It can be divided into four classes: double-tagging, single-tagging, no-tagging and anti-tagging.

Typical small angle taggers cover an angular range between about 20 and 100 mrad, while the very small angle taggers cover the range of about 3 to 15 mrad.

Double-tagging

Double-tagging is when both the scattered leptons are detected. With their energies as well as scattering angles determined, it is possible to calculate the four-momentum vectors of both photons, and have the full reaction kinematics available for *e.g.* precise cross section studies or better determination of the x dependence of the Photon Structure Function.

The invariant mass of the particle system seen in a detector will be less than that given by equation (4.5). Some particles will go undetected inside the beam pipe. To translate the *visible* invariant mass to the *true* one, when not tagging both scattered beam particles, one must go through a complicated unfolding procedure. With increasing energy the relation between $W_{visible}$ and W_{true} gets worse. More particles go undetected in the beam pipe [30].

Using the double tag method, where both scattered leptons are detected and their four-momenta calculated, the full reaction kinematics is available. The invariant mass can be calculated from the deduced photon four-momenta and Monte Carlo studies show good agreement between W_{true} and W_{tag} from the tagged system above a W of 40 GeV [31]. This means that there is little need to apply unfolding procedures in this region, and extraction of the total $\gamma\gamma$ cross section $\sigma_{\gamma\gamma}$ is possible in a wide region.

Double-tagging also ensures a complete dominance of the two-photon diagram over other competing processes. Due to the strong forward peaking of the scattered leptons, tagging needs to be done at very small angles, typically a few mrad for a reasonable rate of events. High-rate background sources, such as small angle Bhabha scattering, can be difficult to reject without imposing strong cuts that also cut away most of the signal. The experimentally visible cross section for double-tagged two-photon events is very small at LEP1 energies.

Single-tagging

In this case, either of the two scattered leptons is detected. This allows a measurement on the Q^2 of the virtual photon which probes the target photon structure, given by the tagged lepton. By use of single-tagging at different angles, thus different Q^2 values, it is possible to study *e.g.* the Q^2 and x dependences of the photon structure function F_2^γ.

To enter into the deep inelastic scattering range, large Q^2 values are required. This implies either rather large scattering angles ($\theta > 100$ mrad), where the cross section is comparatively low due to the strong forward peaking of the leptons, or going to higher energies, *e.g.* LEP2. When moving to the low Q^2 range ($\theta < 30$ mrad) the event rate increases, and by analysing relatively high-$W_{\gamma\gamma}$ events it is possible to study the production and properties of jets with high transverse momenta $p_\perp$. Resonance production studies can also be carried out with single-tagged two-photon events. Different background sources, like *e.g.* e^+e^- annihilation, can be reduced by the single tag method.

The experimentally visible cross section for single-tagged two-photon events is much higher than that for double-tagged. The ratio between single-tag and double-tag is somewhere between 10 and 100.

No-tagging

The third method is when none of the scattered beam particles are detected, and the only source available for information is the produced particle system. This means that the scattered leptons either go in the beam pipe, or in the hole between the very forward and the forward taggers, and usually implies small momentum transfers. It is necessary to require low Q^2 scattering in order to ensure a dominance of the two-photon process over other reactions, *e.g.* virtual bremsstrahlung with scattering. The no-tag events can be used to study *e.g.* high- and low-$p_\perp$ jets, resonances *etc.*

The visible cross section for no-tag events is at least a factor 100 larger than that of double-tag events.

Anti-tag

In order to avoid contamination from virtual photons in the single-tag and no-tag cases, it is necessary to require the untagged leptons to have small scattering angles, and, thus, low momentum transfer. This can be achieved by using an anti-tag requirement. This means that an event is rejected if two leptons are the detected for the single tag case, and one or two for the no-tag case. By having a tagger covering the very forward region this assures a very low Q^2 for the untagged leptons.

4.2 Two-Photon Physics at DELPHI

Single-tagged and no-tagged two-photon events have been studied for some time by the DELPHI collaboration. Various attempts have been made at looking for double-tagged events, but the LEP integrated luminosity has not been large enough to have a significant data sample until lately.

DELPHI has three forward electromagnetic calorimeters that allow tagging of two-photon data. This gives a large Q^2 range and different aspects of the photon can be studied. The deep inelastic scattering theory can be tested by use of high-Q^2 events, while the low-Q^2 events can be used for studying the perturbative QCD resolved photon processes. The ranges in polar angle and the average Q^2 of the different taggers can be seen in table 4.1.

Table 4.1: Angular ranges and average Q^2 values for the different taggers in DELPHI. Though the SAT detector has been replaced by STIC, it has b een used for two-photon analysis and is listed for that reason.

Tagger	θ [mrad]	$\langle Q^2 \rangle$ [GeV^2]
FEMC	175 - 637	80
SAT	43 - 135	12
STIC	29 - 185	10.4
VSAT	3 - 15	0.06
no-tag	$<$ 43(SAT)	0.12

As can be seen in the table, the no-tag events are anti-tagged by the SAT(STIC) and FEMC, but not by the VSAT. This gives it a higher average Q^2 than the VSAT tagged events.

This section will give a brief introduction to no-tag and VSAT single-tag results obtained by the DELPHI Collaboration. It will also discuss a measurement of the Photon Structure Function F_2^γ made by use of SAT single-tag events. Finally the results of the VSAT double-tagged event study is presented.

4.2.1 Results of No-Tagged Data Analysis

In this analysis, data taken during the LEP runs of 1990-1992 was used, corresponding to an integrated luminosity of about 32 pb^{-1} [41]. Minimum bias data and a sample of events with jets at high-$p_\perp$ were selected under the requirement that no scattered electrons or positrons were detected. The additional cuts for selecting the high-$p_\perp$ jet sample from the minimum bias sample were the requirement of two jets with $p_\perp > 1.75$ GeV/c and polar angles in the range 40° to 140°.

After background subtraction and efficiency corrections, the values for the visible cross section obtained for the two samples were

$$\sigma^{exp}_{\gamma\gamma(I)} = 573 \pm 5(stat) \pm 19(syst)\text{pb}$$
$$\sigma^{exp}_{\gamma\gamma(II)} = 12.8 \pm 0.7(stat) \pm 0.4(syst)\text{pb}$$

where (I) is the minimum bias sample, and (II) is the high-$p_\perp$ jet sample. Comparisons with Monte Carlo generated events of the QPM and VDM models showed that their incoherent sum was not sufficient to describe the data. With the QCD-RPC model included in the sum, agreement between Monte Carlo and data was obtained. A number of different parametrizations of the parton density functions were used, with the result that the Gordon-Storrow (GS) and Levi-Abramowicz-Charchula (LAC1) parametrizations

produced reasonable agreement in most distributions, whereas Drees-Grassie (DG) and Duke-Owens (DO) were too soft and failed to describe the data in the high-$p_\perp$ region.

4.2.2 Results of VSAT Single-Tagged Data Analysis

This analysis was based on VSAT single-tagged two-photon events, using data collected during the LEP runs of 1991 and 1992 [42]. The average Q^2 of the selected events was $\langle Q^2 \rangle = 0.06$ GeV$^2/c^4$.

Monte Carlo samples of the VDM, QPM and QCD-RPC models were generated, and used in order to understand the kinematics of the VSAT tagged $\gamma\gamma$ events. The events of the QCD-RPC model were initially generated with low values of $p_\perp^{min}$, which were then increased until the total VDM+QPM+(QCD-RPC) simulation reproduced the observed number of data events.

Statistical comparisons between data and simulated distributions were performed using two independent methods: the χ^2 test and the Kolmogorov test. The measure of compatibility between the two distributions was given as a probability, $\mathcal{P}$, where a $\mathcal{P}$ value close to 1 indicates very similar distributions, whereas a value near 0 shows an unlikeliness that the two arose from the same parent distribution.

It was clear that the sum VDM+QPM cannot provide a good description of the the data distributions. However, adding the QCD-RPC component generated using either of the PDF parametrizations GS, DG, DO, or LAC1, gave a reasonable description of the data. Further attempts to distinguish between different parametrizations were also made using an overall χ^2-test with several distributions taken into account simultaneously. The results of this was that the GS, DG and LAC1 parametrizations provided a satisfactory description of the data, whereas the DO parametrization was unsufficient.

4.2.3 Measurement of the Photon Structure Function

This analysis was done using SAT single-tagged two-photon events from the LEP runs of 1991-1993. The photon structure function F_2^γ was measured in the Q^2 range from 4 to 30 GeV$^2/c^4$ and down to x values of order 0.001 [43]. A comparison was made with several F_2^γ parametrizations with special emphasis on their low x behaviour. This analysis also presented in appendix D.

When measuring the photon structure function it is necessary to use an unfolding method to find the true x distribution from the visible one. This is done by the following scheme. An event sample is generated with a given $F_2^\gamma(x)$ dependence, and used in order to get the correlation between the true and visible x values. The program used for unfolding treats the x values of data and Monte Carlo through histograms. The unknown function $F_2^\gamma(x)$ is parametrized as a linear sum of spline functions multiplied by coefficients to be determined. The number of bins in the histograms and number of spline functions is defined by the user. For each simulated event the program determines a weight in order to find the best fit to the $x_{visible}$ data distribution. The unfolded result of F_2^γ is then represented in the form of a histogram with the number of bins chosen to minimize their statistical correlations. The simulated events, weighted by the result of the unfolding, have then to reproduce data distributions which were not explicitly involved in the unfolding,

so called control histograms.

A test of both the unfolding and tagging methods was made by studying lepton pair production in order to obtain the known $F_2^{\gamma,QED}$. The muon pair production in the single-tagged two-photon interactions was used for this study. The study of $F_2^{\gamma,QED}$ also gave an opportunity to test the model on influence of the squared mass of the target photon, P^2, on the unfolded result. The value of P^2 which gave the best fit to the measured $F_2^{\gamma,QED}$ was found to be 0.04 GeV$^2/c^4$.

The result of $F_2^{\gamma,QCD}$ obtained is well compatible with results from the OPAL experiment, and the value for the x region of $0.3 < x < 0.8$ agrees well with other experiments as well as QCD predictions.

Also, simulations of various F_2^{γ} parametrizations were compared with the data in the very low x-region, in order to see if any of them could be ruled out. The result of this was that at LEP1 we cannot reach low enough in x to be able to rule out all but one parametrization.

4.2.4 Double-Tagged Two-Photon Data analysis

Double-tagged two-photon events, using the VSAT detector as tagger, could be very useful for *e.g.* cross section measurements, and extraction of the photon structure function F_2^{γ}. This, of course, demands reasonable statistics in order to have small errors. For the case of LEP1, the total integrated luminosity is unfortunately not enough to do any accurate measurements. However, it is possible to study the double-tagged events and find the dominating background sources that will contaminate the event sample.

The analysis was performed on data from 1991-1993 corresponding to a total luminosity of 48.7 pb^{-1}. Monte Carlo simulations of the VDM, QPM and QCD-RPC models were made, and analysed using the same acceptance cuts as applied to the data sample. The sum of the three models was then compared to the data. For the QCD-RPC part two different parametrizations of the parton density function were used, Gordon-Storrow (GS) [44], and Drees-Grassie (DG) [45]. These parametrizations have a limit Q^2_{min}, which is the lower limit of the Q^2 range in which they were evaluated. In the event generation it is possible to use a parameter $p_\perp^{min}$, where $(p_\perp^{min})^2$ should be larger than Q^2_{min} for the generation to be valid, which sets a lower limit for the $p_\perp$ of the events. This cut is necessary to stay above the non-perturbative VDM region and avoid double counting. Normal $p_\perp^{min}$ values very between 1.5 and 3.0 GeV$/c^2$.

This analysis is preliminary. All background sources have not yet been studied fully, due to the low statistics of the data sample. There may be some contamination from $\gamma\gamma \to \tau^+\tau^-$ events in the final data sample. Also, having a very small sample, there has been no investigation of trigger efficiencies and other sources of systematic errors.

Event Selection

There were a few selection criteria for charged tracks and neutral particles in an event. The remaining particles were then considered for some additional event selection cuts. The double-tagging criteria were applied to the events that remained after these first cuts, to give the final number of events accepted as double-tagged two-photon events. Charged particle tracks in the detector were accepted if the following criteria were met:

- particle momentum above 0.4 GeV/c,
- relative error on momentum measurement less than 100 %,
- projection of the impact parameter along the beam direction less than 10 cm,
- radial projection of the impact parameter relative to the interaction point less than 4 cm,
- polar angle in the range $20^\circ < \theta < 160^\circ$,
- error on measurement of radial projection of the impact parameter below 2 cm,
- error on measurement of the impact parameter along the beam direction below 5 cm.

The calorimetric information was used for selection of neutral particles. Taking into account the sensitivity, stability, and noise performance of the calorimeter, the following threshold were chosen for measured energy: 0.5 GeV for the FEMC and HPC, and 1.5 GeV for the HAdron Calorimeter (HAC).

The following criteria were used for the event selection, using particles that passed the above mentioned criteria for charged and neutral particles:

- at least 3 charged particles in the event,
- net charge of the observed charged particles not more than two units,
- total visible energy (including the energy of the tagged leptons) below 100 GeV.

The last cut having 100 GeV maximum instead of $2E_{beam}$ is due to the energy resolution of the VSAT detector which is $35\%/\sqrt{E}$.

The selection criteria applied to the leptons tagged by the VSAT detector were:

- preselection using a polar angle range of the detector, 2 mrad $< \theta <$ 25 mrad,
- energy of hit in VSAT above 20 GeV,
- y-position of hit reconstructed in the y-strip plane,
- x-position reconstructed in at least one of the two x-strip planes.

The θ and ϕ angles of the hit are then translated into the production angles of the scattered leptons. If this backtracking through the quadrupoles fails, the event is skipped. Then the number of accepted tags has to be two, *i.e.* neither of the leptons may fail the above cuts.

We now have two accepted lepton tags. However, they have to be on different sides of the interaction point for the event to be a double-tagged two-photon event. It may happen that we have a single-tagged event with an off-momentum beam particle on the same side as the tagged lepton, and these events are cut away. The coincidence of a single-tag event with an off-momentum particle on the opposite side of the interaction point can, of course, also occur. These events are more difficult to distinguish from double-tag events. However, the probabilities of having the off-momentum particle on the same side of the

interaction point as the tagged lepton, or the opposite side, are equal. Thus, the cut on the case where the two particles are on the same side gives as an estimate of the background from the other case.

The final cut is to reduce background from Bhabha scattering in coincidence with some activity in the DELPHI detector. This is done by looking at three key parameters of Bhabha events. The first is the energy of the detected particle that for a bhabha electron must be above 70% of the beam energy. The second is the so called Delta(x) parameter which is the mathematical difference of the x-strip hits of both particles, *i.e.* $x_{hit1} - x_{hit2}$. With perfectly symmetrically placed detector modules, beam displacements equal to zero, and no initial/final state radiation, this difference should be zero. In real life, however, the beam displacement is rarely zero, and the detectors modules are not symmetrically placed, so this Delta(x) parameter is not zero. It gives instead a narrow gaussian distribution, figure 4.7. The third parameter is the Delta(y) which is analogous to Delta(x), and also gives a narrow gaussian distribution, figure 4.8.

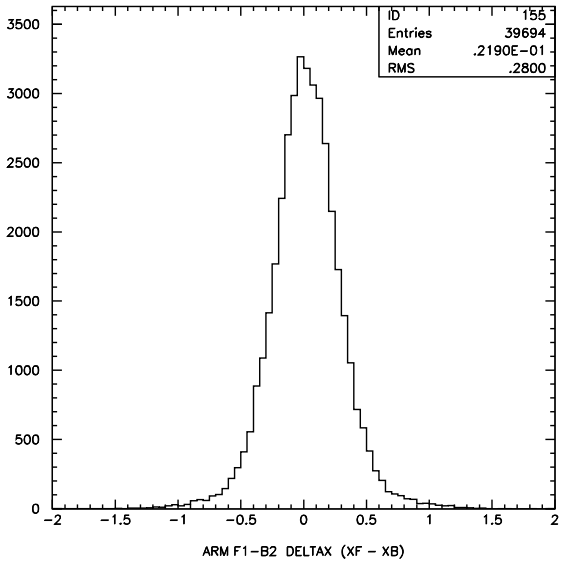

Figure 4.7: Delta(x) distribution of Bhabha scattering events. The x-axis shows Delta(x) in units of cm, and the y-axis shows number of entries.

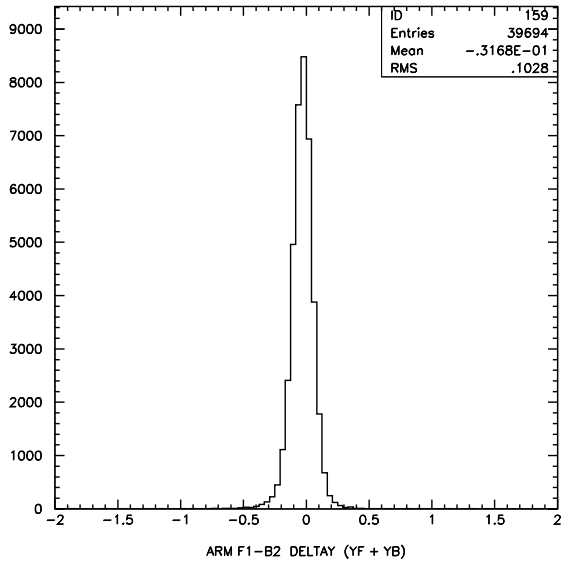

Figure 4.8: Delta(y) distribution of Bhabha scattering events. The x-axis shows Delta(x) in units of cm, and the y-axis shows number of entries.

For events where the tags are in two modules of a bhabha diagonal, the cut applied is to have the measured energy below 70% of the beam energy, Delta(x) value outside the range Delta$(x)_{bhabha} \pm \sigma$(Delta$(x)_{bhabha}$), and the Delta(y) value outside the range Delta$(y)_{bhabha} \pm \sigma$(Delta$(y)_{bhabha}$), where Delta$(x)_{bhabha}$ and Delta$(y)_{bhabha}$ are the average values of the distributions for bhabha events, and σ is their respective widths. Since the average values of these distributions depend strongly on beam parameters such as beam displacement and tilt, it is necessary to obtain an average value for each LEP fill and compare the two-photon events to the values of the fills in which the events are found.

For the Monte Carlo simulations, a big sample of Bhabha events was generated with the same beam parameters as the two-photon events, and the Delta(x) and Delta(y) distributions thus obtained were used for the cuts.

To give an indication on how the different selection criteria reduce the data samples, table 4.2 lists the remaining number of events in the data samples after different cuts. The first row shows the initial number of events in the analysed samples, which has been subjected to a preselection with much looser cuts on the DELPHI particle system than are listed above, and with no tag requirements. The individual cuts on charged particle tracks and neutral particles are not listed in the table. The first cut listed as *Track quality* is the sum of all these criteria, and shows a reduction of about 75% of the number of events. The criteria on the individual VSAT hits, *i.e.* $E_{tag} > 20$ GeV, y- and x-positions reconstructed, backtracking through the quadrupole magnets, and two hits pass ing these cuts, are all included in the *Cuts on VSAT hits* entry in the table. Finally, *Bhabha cut* is the selection criteria that rejects the events which passes the normal cuts for the analysis of Bhabha events.

Table 4.2: The effect on the data samples by the different selection criteria.

Selection Criterion	Data Sample		
	1991	1992	1993
Initial events	6747	10925	11540
Track quality	1207	2904	3011
≥ 3 charged particles	1097	2596	2707
Net charge ≤ 2	947	2125	2289
Cuts on VSAT hits	4	38	26
Bhabha cut	3	24	12
$E_{vis} < 100$ GeV	2	8	5

It is seen in table 4.2 that the largest reduction is by the criterion that requires that we have hits in two of the VSAT modules in coincidence with a particle system in the DELPHI detector. The criterion that the total visible energy should be less than 100 GeV also gives a big reduction of the samples.

Results and Discussion

There is a total of 15 double-tagged events found in the data sample from 1991-1993. Thus, the statistical error is 25%, and it is therefore very hard to estimate a sensible systematic error for the analysis. These data events are then compared to Monte Carlo predictions of the two-photon process. The generator used in the simulations was the TWOGAM generator [46], which was developed by members of the DELPHI collaboration.

From the Monte Carlo generated samples, it is possible to calculate the effective cross section of each model, by using the corresponding luminosity and number of events that pass the selection criteria. The detector simulation was changed slightly in 1993 meaning that the data samples of 1991 and 1992 should be compared to one version of the detector simulation, while 1993 should be compared to another. This gives the effective cross sections for the Monte Carlo samples as shown in table 4.3.

This can be taken one step further in calculating the expected number of events for the Monte Carlo models for each year of data that was analysed. Then, forming the sum QPM+VDM+(QCD-RPC), one can compare it to the number of events actually found in

Table 4.3: The effective cross section of different Monte Carlo samples that have been run through different versions of the detector simulation.

Monte Carlo Model	Simulation Version	Luminosity [pb^{-1}]	Number of events	σ_{eff} [pb]
VDM	1991	983.7175	236	0.2399
QPM	1991	5294.5393	46	0.0087
QCD-GS, $p_\perp^{min} = 1.8$ GeV/c	1991	1432.9723	112	0.0782
QCD-GS, $p_\perp^{min} = 1.6$ GeV/c	1991	881.6515	91	0.1032
QCD-GS, $p_\perp^{min} = 1.9$ GeV/c	1991	1782.0618	102	0.0572
QCD-DG, $p_\perp^{min} = 1.4$ GeV/c	1991	1168.6881	93	0.0796
QCD-DG, $p_\perp^{min} = 1.5$ GeV/c	1991	1491.4285	91	0.0610
QCD-DG, $p_\perp^{min} = 1.6$ GeV/c	1991	1875.3811	98	0.0523
VDM	1993	983.7175	230	0.2338
QPM	1993	5294.5393	52	0.0098
QCD-GS, $p_\perp^{min} = 1.8$ GeV/c	1993	1432.9723	119	0.0830
QCD-GS, $p_\perp^{min} = 1.6$ GeV/c	1993	881.6515	101	0.1146
QCD-GS, $p_\perp^{min} = 1.9$ GeV/c	1993	1782.0618	98	0.0550
QCD-DG, $p_\perp^{min} = 1.4$ GeV/c	1993	1168.6881	88	0.0753
QCD-DG, $p_\perp^{min} = 1.5$ GeV/c	1993	1491.4285	87	0.0583
QCD-DG, $p_\perp^{min} = 1.6$ GeV/c	1993	1875.3811	97	0.0517

the data. Table 4.4 shows the expected number of events from the model sum for different years and different parametrizations of the QCD-RPC model, and the number of events found in data. There is also one entry 'No QCD-RPC', which shows the expected number of events from QPM+VDM, *i.e.* without any QCD-RPC model.

Table 4.4: The expected number of events from QPM+VDM+(QCD-RPC) for different parametrizations of the QCD-RPC part, and for years 1991, 1992 and 1993, compared to the number of events found in the data samples.

QCD-RPC parametrization	Data Sample		
	1991	1992	1993
QCD-GS, $p_\perp^{min} = 1.8$ GeV/c	2.3	6.3	7.3
QCD-GS, $p_\perp^{min} = 1.6$ GeV/c	2.5	6.7	8.1
QCD-GS, $p_\perp^{min} = 1.9$ GeV/c	2.2	5.9	6.7
QCD-DG, $p_\perp^{min} = 1.4$ GeV/c	2.3	6.3	7.2
QCD-DG, $p_\perp^{min} = 1.5$ GeV/c	2.2	5.9	6.8
QCD-DG, $p_\perp^{min} = 1.6$ GeV/c	2.1	5.8	6.6
No QCD-RPC	1.8	4.8	5.7
Data	2	8	5

We can clearly see that the statistics are far too low to say anything about which QCD-RPC parametrization describes the data best. Neither can we really say that we need the QCD-RPC model to explain the number of events found in the data samples. We have not investigated all background sources yet, and some background from the $\gamma\gamma \to \tau^+\tau^-$ process can be expected. However, it has been shown previously in the case

of VSAT single-tag data that the QCD-RPC contribution to the sum is needed [42] in order to explain the distributions of the data, and it is a fair assumption that this is valid also in the case of VSAT double-tag data.

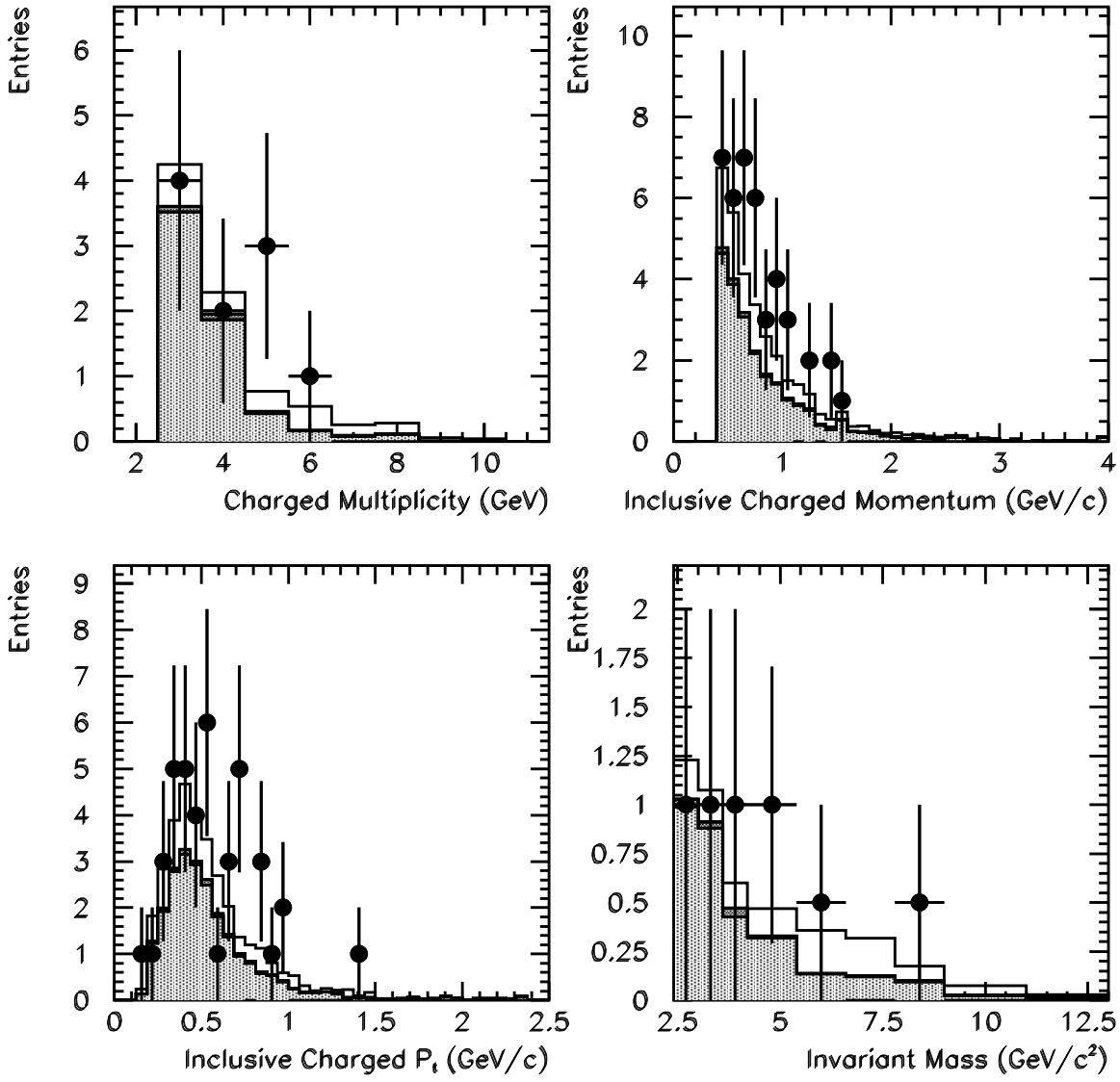

Figure 4.9: Charged momentum, inclusive charged momentum, inclusive charged $p_\perp$, and invariant mass of the hadronic system. The data is represented by points. The unhatched histogram shows QPM+VDM+(QPC-RPC), the darker hatched is the QPM+VDM sum and the lighter hatched is the VDM model. The difference between QPM+VDM and VDM is very small.

A few distributions were chosen from the data sample from 1991-1992 and the sample from 1993, where the data is compared to Monte Carlo simulations. Figure 4.9 shows four plots, the charged multiplicity, inclusive charged momentum, inclusive charged $p_\perp$, and invariant mass of the hadronic system for 1991 and 1992 combined. The invariant mass is calculated using the particles in the hadronic system, and we have not used the

information of the four-momenta of the photons that can be deduced from the tagged particles.

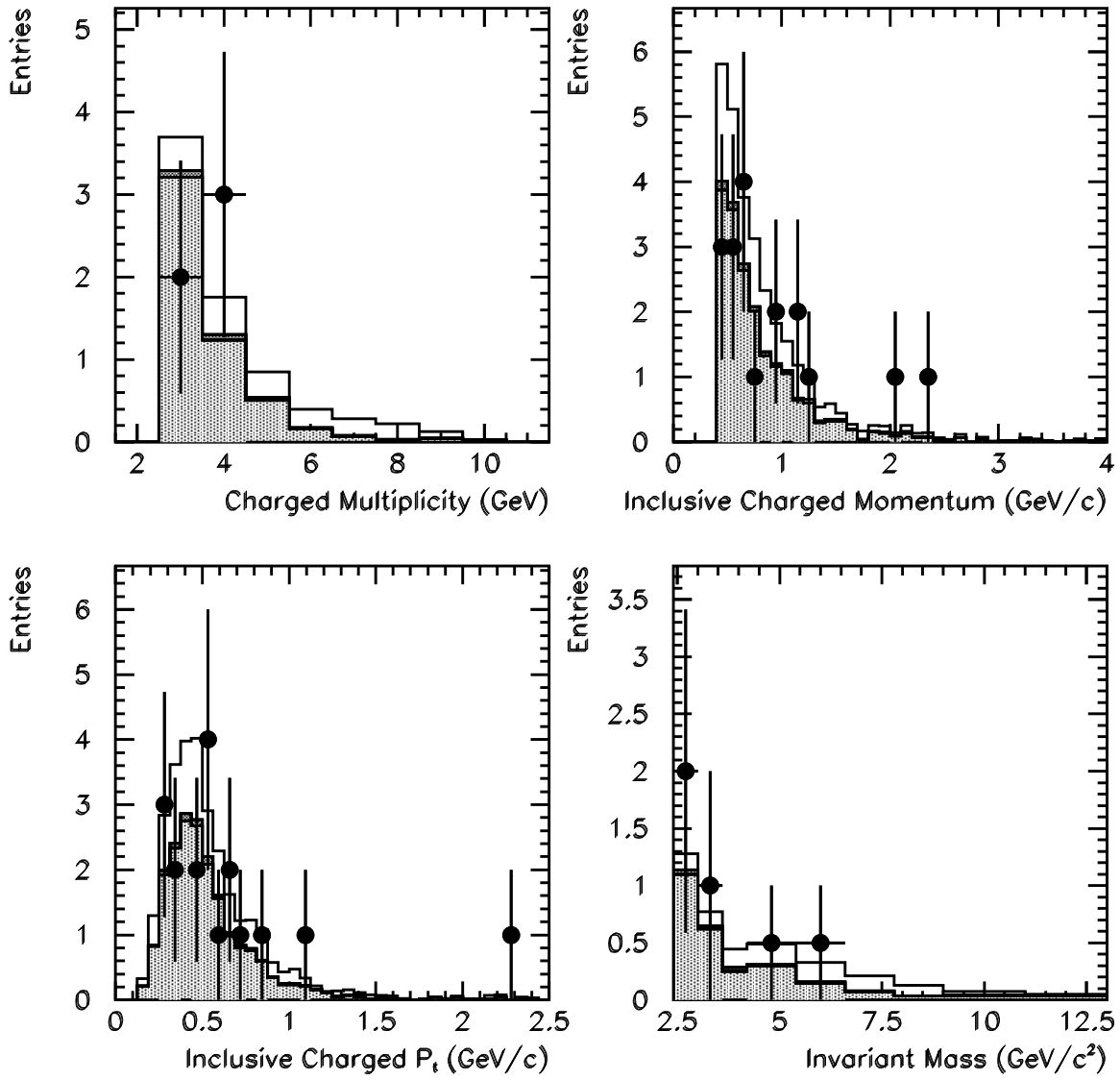

Figure 4.10: Charged momentum, inclusive charged momentum, inclusive charged $p_\perp$, and invariant mass of the hadronic system. The data is represented by points. The histograms are as before.

We also want to show the agreement between Monte Carlo and the data sample from 1993. Figure 4.10 shows the same four distributions as figure 4.9. This data sample contains only five events and that is far too few to make any firm statements on the agreement between data and Monte Carlo. The statistical uncertainties cover any possible combination of Monte Carlo models that we can use.

The distributions from data and Monte Carlo show a reasonably good agreement, but with such low statistics it is hard to say if the QCD-RPC model really is needed. The QPM+VDM sum, or even VDM only, is sufficient to explain the data distributions within

the statistical uncertainties. The plots in figures 4.9 and 4.10 were made using the QCD-GS model with $p_{\perp}^{min} = 1.8$ GeV/c. Other parametrizations of the parton density function give similar agreement with data.

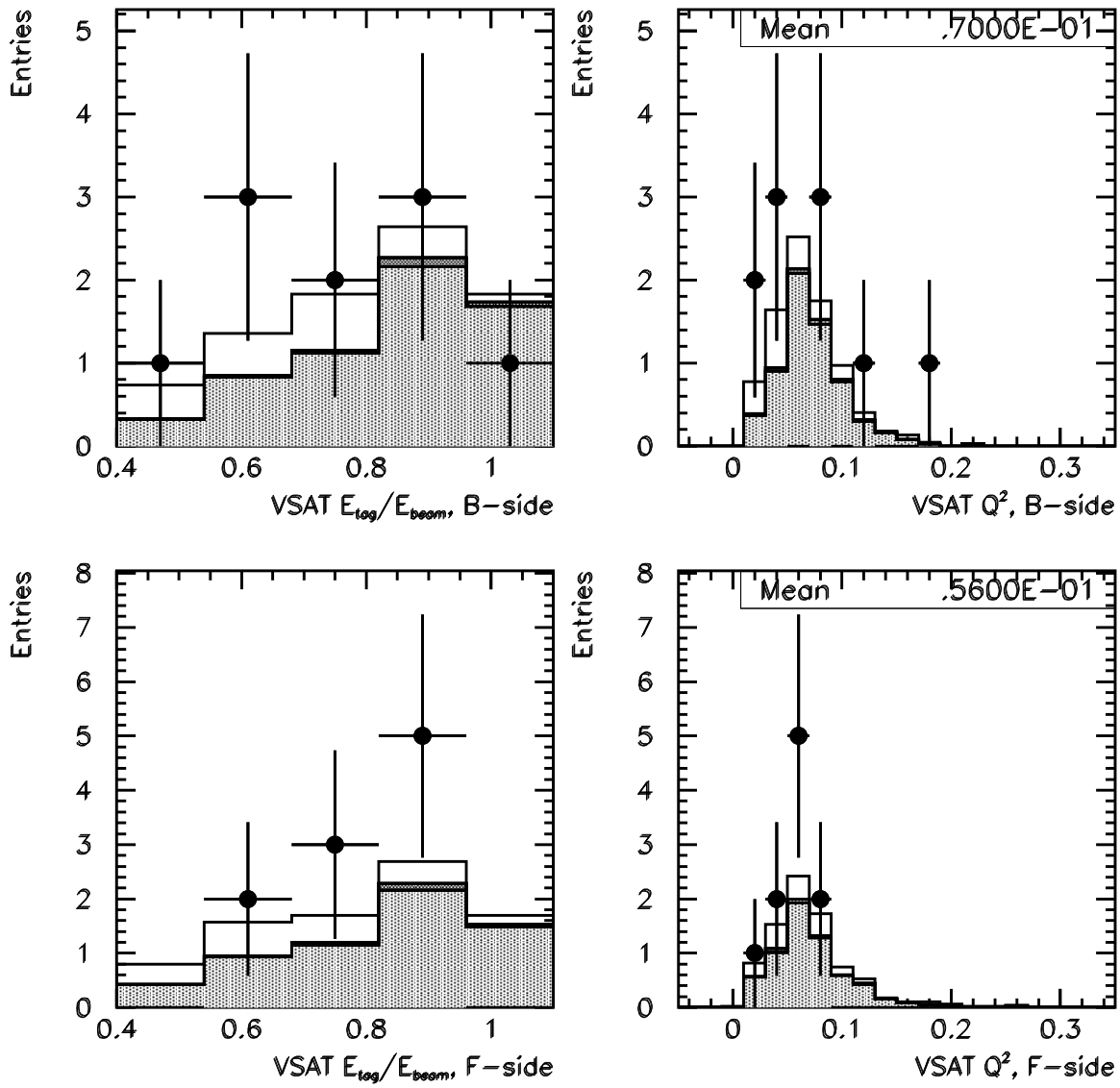

Figure 4.11: E_{tag}/E_{beam} and Q^2 distributions for the B- and F-side, where the F-side corresponds to electrons and B-side to positrons tagged by the VSAT. Data from 1991 and 1992.

We also want to make sure that the data distributions of the tagged leptons are in agreement with Monte Carlo simulations. Figure 4.11 shows the distributions of the E_{tag}/E_{beam} and the Q^2 for the B- and F-sides. When looking at single-tag data it is customary to call the momentum transfer of the photon coming from tagged lepton Q^2, while for the target photon it is called P^2. When looking at double-tagged data it is not clear what to call the momentum transfer of the different photons. One could make a distinction of always calling the larger of the two Q^2 and the other P^2. I have here chosen to distinguish the photon coming from the electron and that from the positron, the F-side

corresponding to the electron. This gives us the two different $\langle Q^2 \rangle$ values that are seen in figure 4.11. The same convention is used for histogram representation as in figure 4.9, *i.e.* the unhatched histogram is the sum QPM+VDM+(QCD-RPC), the darker hatched is QPM+VDM, and the lighter hatched is VDM only.

The data and Monte Carlo agrees reasonably well within the statistical errors. These plots may, however, give a stronger indication for the need of the QCD-RPC model in describing the distributions of the data sample. The average Q^2 of the two sides are 0.07 GeV$^2/c^4$ for the B-side and 0.06 GeV$^2/c^4$ for the F-side. The same distributions for 1993 data look quite similar, but with slightly different $\langle Q^2 \rangle$ values. Summing up all three years of data and extracting the $\langle Q^2 \rangle$ for all 15 events we arrive at 0.07 GeV$^2/c^4$ for the B-side and 0.06 GeV$^2/c^4$ for the F-side, figure 4.12.

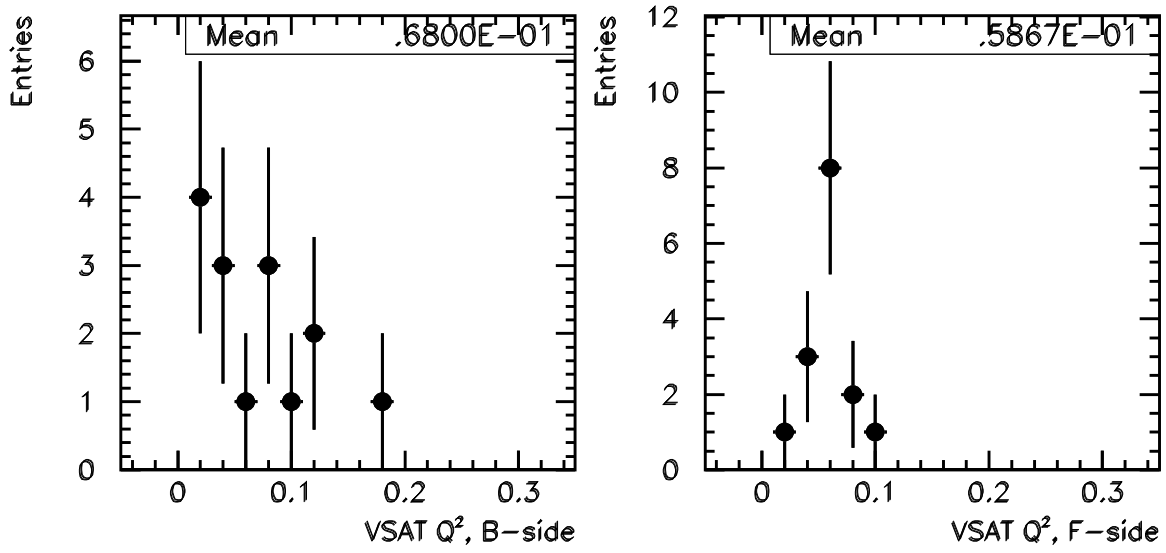

Figure 4.12: Q^2 distributions for the B- and F-sides, where the F-side corresponds to electrons and B-side to positrons tagged by the VSAT. Data from 1991-1993.

Summary

An analysis of VSAT double-tagged two-photon data taken during the LEP runs of 1991-1993 has been made. The total luminosity of the sample is 48.7 pb^{-1}, and a total of 15 events were found. This is used for calculating the cross section for the VSAT double-tag analysis. The result is

$$\sigma^{\gamma\gamma}_{double-tag} = 0.31 \pm 0.08(stat) \text{ pb}. \tag{4.28}$$

This result is preliminary. Since the statistical error is so large, the error on the luminosity is negligible . A few things would be worth doing once the data sample from 1994 is included:

- full background study,
- trigger efficiency evaluation,

- error on luminosity measurement should be included,

This study shows that it is possible to do a double-tag analysis using the VSAT as tagger in a very small angular range 3 to 15 mrad. This is promising for the LEP2 phase, where the expected two-photon data sample will be large enough for cross section measurements and comparisons of this with predictions of the models.

Acknowledgement

I wish to thank my supervisor, Professor Göran Jarlskog, for supporting me in every way and giving me a chance to pursue a Ph.D. in Particle Physics.

DELPHI is indeed a very large collaboration, and success depends heavily on the efforts of a large number of people. I therefore wish to thank the whole collaboration for making the present thesis possible at all.

There are a few people within the collaboration that I would like to thank explicitely for all their support when either working with the on-line system of VSAT, or when performing analysis of data. Firstly, I wish to thank Giuseppina Rinaudo, Ulf Mjörnmark, and Henrik Carling for giving a helping hand with the VSAT data aquisition system whenever problems appeared.

I thank Gian Gopal and Yura Belokopytov for their help in understanding and using the DELPHI data base system. Robert Sekulin, Tim Adye, Gareth Smith, Mark Dönszelmann, and André Augustinus of the DELPHI DAS group and Alex Read, Steinar Stapnes, and Bernhard Skaali of the SAT group have provided a helping hand in setting up the VSAT slow control system. Also mentioned should be Philippe Charpentier and Philippe Gavillet for their assistance with the on-line soft- and hardware when I was 'in charge' of the VSAT detector during 1991 and 1992.

When learning about and analysing two-photon data I have been fortunate to work closely with Nikolai Zimin. I also want to thank Frederic Kapusta of the two-photon physics team for fruitful discussions. I am greatly indebted to Torbjörn Sjöstrand for his patience and help in trying to understand the theory behind two-photon physics.

Many thanks to everybody at the Department of Elementary Particle Physics in Lund. Especially to Olof Bärring for solving many of my programming bugs, Björn Lundberg and Henrik Carling for teaching me some basics in electronics (and all our games of xblast), Ulf Mjörnmark and Sverker Almehed for their exceptional performance in taking care of the computer system, Jonas Bjarne and Lars Jönsson for being my interpreters during my first year in Geneva, Per Jonsson for reminding me a lot of facts about the VSAT detector, and Vincent Hedberg for building a swimming pool and letting me use it.

Finally, thanks to my old friends Edvin, Mats, and Wibbe for the good times and many laughs shared outside working hours.

Financial support from the Lund University is gratefully acknowledged.

Bibliography

[1] DELPHI Collaboration, P.Aarnio *et al.*, Nucl. Instr. Methods **A303** (1991) 233.

[2] N.Bingefors *et al.*, Nucl. Instr. Methods **A328** (1993) 447;
V.Chabaud *et al.*, Nucl. Instr. Methods **A368** (1996) 314.

[3] F.Hartjes *et al.*, Nucl. Instr. Methods **A256** (1987) 55.

[4] C.Brand *et al.*, IEEE Trans. Nucl. Sci. **NS-36** (1989) 122;
C.Brand *et al.*, Nucl. Instr. Methods **A283** (1989) 567;
Y.Sacquin, Contribution to the proceedings of the VIth International Wire Chamber Conference, Vienna;
L.Chevalier, Thèse, Université Paris Sud, July 20 1992;
G.Hamel de Monchenault, Thèse, DAPNIA/SPP 92-11;
O.Bärring, Thesis, Lund Univ., LUNFD6/(NFFL-7071)1992.

[5] A.Amery *et al.*, Nucl. Instr. Methods **A283** (1989) 502.

[6] W.Bartl *et al.*, Nucl. Instr. Methods **A337** (1994) 295.

[7] M.Berggren *et al.*, Nucl. Instr. Methods **A225** (1984) 477;
H.G. Fischer, Nucl. Instr. Methods **A265** (1988) 218.

[8] A.Firestone, DELPHI 91-111 CAL 83 (1991) unpublished;
P.Yepes, DELPHI 92-39 GEN 128 CAL 90 (1992) unpublished.

[9] P.Checcia *et al.*, Nucl. Instr. Methods **A275** (1989) 49.

[10] S.J.Alvsvaag *et al.*, Proceedings of the 6th Meeting on Advanced Detectors, La Biodola, Elba, Italy, May 1994, DELPHI 94-126 CAL 117;
S.J.Alvsvaag *et al.*, Proceedings of the 5th International Conference on Calorimetry, Brookhaven National Laboratory, USA, September 1994, DELPHI 94-148 CAL 118;
S.J.Alvsvaag *et al.*, Proceedings of the 4th International Conference on Advanced Technology and Particle Physics, Como, Italy, October 1994, Nucl. Phys. B (Proc. Supp.), DELPHI 95-12 CAL 119.

[11] S.Almehed *et al.*, Nucl. Instr. Methods **A305** (1991) 320.

[12] Ph.Charpentier, Proceedings of the CHEP conference, Tsukuba, March 11-18 1991, DELPHI 91-92 DAS 112;
M.Jonker, Proceedings of the CHEP conference, Tsukuba, March 11-18 1991, DELPHI 91-93 DAS 113.

[13] J.Barlow *et al.*, IEEE trans. nucl. sci. **36** (1989) 1549.

[14] Yu.Belokopytov, V.Perovozchikov, DELPHI 90-36 PROG 153 (1990) unpublished;
Yu.Belokopytov, V.Perovozchikov, DELPHI 93-5 PROG 195 (1993) unpublished.

[15] Yu.Belokopytov *et al.*, DELPHI 90-38 PROG 155 (1990) unpublished;
Yu.Belokopytov *et al.*, DELPHI 93-4 PROG 194 DAS 138 (1993) unpublished.

[16] T.J.Adye *et al.*, DELPHI 94-15 DAS 152 (1994) unpublished.

[17] Yu.Belokopytov, S.Gumenyuk, V.Perevozchikov, DELPHI 90-37 PROG 154 (1990) unpublished.

[18] Yu.Belokopytov *et al.*, DELPHI 93-2 PROG 193 DAS 136 (1993) unpublished.

[19] I.Kronkvist, "Userguide to the VSAT online database program package", unpublished.

[20] T.J.Adye *et al.*, DELPHI 93-12 DAS 140 (1993) unpublished;
T.J.Adye *et al.*, Nucl. Instr. and Meth. **A349** (1994) 160;
and expanded with additional technical details in DELPHI 94-14 DAS 151 (1994) unpublished.

[21] Digital Equipment Corporation, VMS System Services Reference Manual, Version 5.5, Maynard, Massachusetts, November 1991.

[22] R.Holm, S.Ström, "PSSAT2 Microcontrolled Power Supplies via RS232", Department of Physics, University of Oslo, unpublished.

[23] H.Carling, "The VSAT Tunnel Processor", LUNFD6/(NFFL-7058) 1990.

[24] PLUTO Collaboration, Ch.Berger *et al.*, Z. Phys, **C26** (1984) 353.

[25] TPC/2γ Collaboration, H.Aihara *et al.*, Phys. Rev. Lett. **58** (1987) 97;
TPC/2γ Collaboration, H.Aihara *et al.*, Phys. Rev. **D41** (1990) 2667.

[26] AMY Collaboration, R.Tanaka *et al.*, Phys. Lett. **B277** (1992) 215.

[27] ALEPH Collaboration, D.Buskulic *et al.*, Phys. Lett. **B313** (1993) 509.

[28] L3 Collaboration, O.Adriani *et al.*, Phys. Lett. **B318** (1993) 575.

[29] OPAL Collaboration, R.Akers *et al.*, Z. Phys. **C61** (1994) 199.

[30] J.R.Forshaw, M.H.Seymour, Proceedings of the Photon '95 International Workshop on Gamma-Gamma Collisions and Related Processes, Sheffield, UK, April 8-13, 1995, CCL-TR-95-006, CERN-TH/95-105 (1995).

[31] Report on '$\gamma\gamma$ Physics', conveners P.Aurenche and G.A.Schuler, in Proceedings Physics at LEP2, eds. G.Altarelli, T.Sjöstrand adn F.Zwirner, CERN 96 01, Vol.1, p. 291.

[32] H.Kolanoski, P.Zerwas, "Two-Photon Physics", High Energy Electron-Positron Physics, eds A.Ali, P.Söding, (1988) p695, ISBN 9971-50-260-7.

[33] G.A.Schuler, T.Sjöstrand, CERN-TH/96-119, LU TP 96-13.

[34] A.Donnachie, P.V.Landshoff, Phys. Lett. **B296** (1992) 227.

[35] PLUTO Collaboration, CH.Berger *et al.*, Phys. Lett. **B149** (1984) 421.

[36] TASSO Collaboration, M.Althoff *et al.*, Z. Phys. **C31** (1986) 527.

[37] CELLO Collaboration, H.J.Behrend *et al.*, Z. Phys. **C51** (1991) 365.

[38] J.Rosner, NBL Report 17522 (1972) 316.

[39] I.F.Ginzburg, V.G.Serbo, Phys. Lett. **B109** (1982) 231.

[40] J.J.Sakurai, D.Schildknecht, Phys. Lett. **B41** (1972) 489.

[41] DELPHI Collaboration, P.Abreu *et al.*, Z. Phys. **C62** (1994) 357.

[42] DELPHI Collaboration, P.Abreu *et al.*, Phys. Lett. **B289** (1992) 199. J.Bjarne, Thesis, Lund Univ., LUNFD6/(NFFL-7089) 1994.

[43] DELPHI Collaboration, P.Abreu *et al.*, Z. Phys. **C69** (1996) 223.

[44] L.E.Gordon, J.K.Storrow, MC-TH 91-29 (1991).

[45] M.Drees, K.Grassie, Z.Phys. **C28** (1985) 451.

[46] S.Nova, A.Olshevski, T.Todorov, 'A Monte Carlo Event Generator for Two Photon Physics', DELPHI 90-35 (1990) unpublished.

Appendix A

A Silicon-Tungsten Electromagnetic Calorimeter for LEP

Appendix B

The Database of the DELPHI Very Small Angle Tagger (VSAT)

Appendix C

The Slow Control Systems of the DELPHI Small Angle Tagger (SAT) and Very Small Angle Tagger (VSAT)

Appendix D

A Measurement of the Photon Structure Function F_2^γ at an Average Q^2 of 12 GeV$^2/c^4$